# Fast simulation of temperature and phase transitions in directed energy deposition additive manufacturing

Daniel Weisz-Patrault

# Fast simulation of temperature and phase transitions in directed energy deposition additive manufacturing

Daniel Weisz-Patrault

*LMS, CNRS, École Polytechnique, Institut Polytechnique de Paris, F-91128 Palaiseau, France*

**Abstract**

In this contribution, a simplified macroscopic and semi-analytical thermal analysis of directed energy deposition (DED) is presented to obtain computationally efficient simulations of the entire process. Solidification and solid-state phase transitions are taken into account. The model is derived for laser metal powder directed energy deposition, although it can be simply adapted for other focused thermal energy (e.g., electron beam, or plasma arc). The gas flow used for carrying the powder significantly influences cooling conditions, which is included in the model. The proposed simulation strategy applies to multilayer composites with a wide range of shapes in the horizontal plane and arbitrary laser scanning strategies (continuous way, back and forth, etc.). The proposed work provides a simple tool to study the influence of most process parameters, design in-situ experiments and in turn develop optimization loops to reach material requirements and specific microstructures. In-situ pyrometer measurements have been compared to the model, and good agreement has been observed with 2.6% error in average. The model is used to demonstrate the effect of various process parameters for a simple cylindrical geometry and a more complex auxetic cell.

*Keywords:* Additive manufacturing, Phase transitions, Heat conduction, Semi-analytical solution

## 1. Introduction

In this paper a thermal analysis of directed energy deposition (DED) [1] is presented. The model is derived for laser metal powder directed energy deposition (LMPDED), although it can be simply adapted for other focused thermal energy (e.g., electron beam, or plasma arc). LMPDED involves injecting a stream of metallic powder that is melted by a laser beam in order to deposit material layer-by-layer on a build platform [2]. Argon is usually used to carry the powder. This technology enables the users to quickly produce complex thin-walled structures such as meta-materials, auxetics, etc. (Similar processes also exist for this purpose [3, 4]). The additive manufacturing field has been intensively studied for a decade (see [5, 6] for reviews of the literature). As the microstructure significantly depends on very local conditions of the melt pool, many papers focus on very detailed simulations of the process, especially powder (e.g., granulometry, flowability, energy absorption, etc.) [7–9], powder melting, the hydrodynamic problem determining the melt pool shape, and cooling and grain growth during crystallization [10–17]. Comprehensive but computationally costly mesoscale simulations [18] include the spreading process of powder, the melting phase and grain growth during solidification.

The main objective of many studies is to link the process parameters of the machine to the final microstructure and residual stresses [19–24], as the ambition is to optimize the mechanical

properties of the manufactured parts. This link is a complex interweaving of coupled physical processes: heat transfer, microstructural evolutions (e.g., phase transitions), plasticity, etc. LM-PDED induces a very specific temperature history including very high temperature gradients and thermal cycling. Both the microstructure formation/evolution and the formation of residual stresses are driven by thermal conditions during the process. Therefore, significant efforts have been made to simulate accurately, at the macroscopic scale, both temperature evolutions and solidification kinetics. However, macroscopic modeling of such processes is computationally costly [20, 23, 25–32], which hinders the development of numerical optimization of the process parameters at the scale of the entire process.

A simplified approach [33] relies on modeling successively cylindrical composites under axisymmetric conditions. This model is unidimensional and heat transfers are limited to the build direction. This structure is simulated numerically by using the finite difference method. Despite the highly simplified geometry, computation times are still limiting for large parts. Indeed, the temperature at each position evolves very rapidly between each layer pass. Therefore, time discretization should be sufficiently thin to capture fast evolutions, especially if rapid phase transitions are also considered.

A semi-analytical model is proposed in this contribution to overcome such difficulties. Indeed, the semi-analytical solution do not rely on time and space discretization and very rapid temperature evolutions are captured without additional computational cost. Of course, the analytical solution should be computed at different times and positions. The choice of the discretization does not affect the results but only the time and space resolution of the outputs.

Several approaches rely on semi-analytical models for selective laser melting (SLM). For instance, a superposition-based finite element approach [34] has been proposed to reduce the computation cost of traditional finite element modeling. A nearly analytical solution for a moving source in a semi-infinite medium is coupled with a coarse finite element analysis to take into account boundary conditions on the finite domain. The superposition of analytical solutions for point heat sources in semi-infinite space, is also used in [35]. Boundary conditions are verified in a finite domain by introducing complimentary numerical/analytical fields. Other similar strategies have been proposed [36–38]. All these approaches are well suited for SLM and exploit the same type of analytical solutions for point heat sources in semi-infinite space and differ mostly on the strategy to verify boundary conditions in the finite domain.

Similar strategies have also been applied to DED in [39], using reflection techniques introduced in [40]. However, such approaches are limited to simple flat-wall geometry. Thus, the simplified thermal analysis proposed in this paper is based on a different strategy to obtain computationally efficient simulations of the entire process. Instead of using analytical solutions for moving point heat sources in semi-infinite space, the approach relies on a semi-analytical solution of the transient heat conduction problem in multilayer composites with proper boundary conditions. Fluxes along the horizontal direction are neglected so that the problem reduces to several two-dimensional (radial and vertical directions) multi-layer composites. The solution derivation extends previous analytical solutions (e.g.,[41, 42]). Although the proposed strategy relies on two-dimensional solutions, pseudo-three dimensional temperature fields are obtained by combining several computations.

Powder melting is not simulated, as molten metal is directly deposited on top of the already existing layers. Thus, the proposed approach does not focus on the hydrodynamic problem in the melt pool. However, solidification and solid-state phase transitions are taken into account. The gas flow used for carrying the powder significantly influences cooling conditions, which

is also included in the model. The part is a superposition of identical layers with a wide range of shapes in the horizontal plane. Geometrical restrictions on the horizontal path are limited to intersection and tangent points. Thus, multi-track structures are excluded and complex geometries cannot be accurately computed near intersection or tangent points. Moreover, the approach applies to arbitrary laser scanning strategies (continuous, back and forth, dwell times, etc.).

The proposed work provides a simple tool to study the influence of process parameters, design in-situ experiments and in turn to develop optimization loops to reach material requirements. In-situ pyrometer measurements have been compared to the model and good agreement has been observed with 2.6% error in average. The model is then used to demonstrate the effect of various process parameters for a cylindrical geometry and a cell of an auxetic structure. The paper is organized as follows. The modeling strategy and assumptions are presented in section 2. The semi-analytic solution is derived in section 3. The phase transition model is presented in section 4. The model is then compared with in-situ experiments in section 5. Several simulations are performed for a simple cylindrical shape in sections 6 and 7. A more complex geometry (auxetic cell) is investigated in section 8 in order to demonstrate the model capabilities. Conclusive remarks are given in section 9.

## 2. Modeling strategy

### *2.1. Basic equations*

Consider a path in the horizontal plane denoted by $\chi$. Consider $\Omega(t)$ the time dependent domain occupied by the body being fabricated and $\Omega_{\text{pla}}$ the build platform. The build platform is fixed in the machine on a platen. As shown in figure 1, the domain is a multilayer structure based on $\chi$. Powder melting is not included in the model. Instead, we consider that the molten metal is directly deposited on the already existing domain. The deposition temperature is adjustable depending on the laser speed and power. Consider $\Gamma(t)$ the extremal zone where the molten metal is deposited, and $\widetilde{\Gamma}(t)$ the area heated by the laser. Notations are depicted in figure 1.

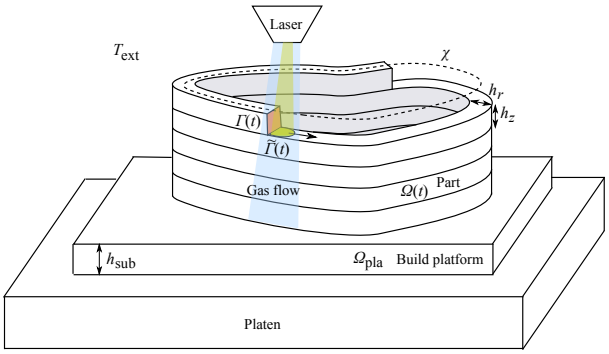


Figure 1: Notations

The heat conduction equation reads:

$$\forall \boldsymbol{x} \in \Omega(t) \cup \Omega_{\text{pla}},\ \text{div}(\lambda(T)\boldsymbol{\nabla} T(\boldsymbol{x},t)) - \rho c_p(T)\frac{\partial T(\boldsymbol{x},t)}{\partial t} = -\sum_{\phi=1}^{N_\phi} \Delta H_\phi(T)\dot{X}_\phi \tag{1}$$

Where $T$ is the temperature, $\boldsymbol{x}$ is the material point, $t$ is the time, $\lambda$ is the thermal conductivity, $\rho$ is the density, $c_p$ is the specific heat capacity, $N_\phi$ is the number of phase transitions (e.g., liquid-solid, austenite-martensite, etc.), $\Delta H_\phi$ is the enthalpy change during the $\phi$-th phase transition, and $\dot{X}_\phi$ are the phase proportion rates. Boundary conditions include the loss of heat due to convection and radiation, and the heat flux applied by the laser (denoted by $q_{\text{beam}}$). Thus, boundary conditions read:

$$\begin{cases} \lambda \boldsymbol{\nabla} T.\boldsymbol{n} = -H\left(T - T_{\text{ext}}\right) - \sigma\epsilon\left(T^4 - T_{\text{ext}}^4\right) & \boldsymbol{x} \in \partial\Omega(t) \cup \partial\Omega_{\text{pla}} - \widetilde{\Gamma}(t) - \Gamma(t) \\ \lambda \boldsymbol{\nabla} T.\boldsymbol{n} = -H\left(T - T_{\text{ext}}\right) - \sigma\epsilon\left(T^4 - T_{\text{ext}}^4\right) + q_{\text{beam}} & \boldsymbol{x} \in \widetilde{\Gamma}(t) \\ T = T_{\text{dep}} & \boldsymbol{x} \in \Gamma(t) \end{cases} \tag{2}$$

Where $\boldsymbol{n}$ denotes the outward normal vector. The initial condition reads:

$$T = T_{\text{ext}} \quad \boldsymbol{x} \in \Omega_{\text{pla}} \quad t = 0 \tag{3}$$

Where $T_{\text{ext}}$ is the room temperature, $T_{\text{dep}}$ is the deposition temperature, $H$ is the heat transfer coefficient , $\sigma$ is the Stefan-Boltzmann constant, and $\epsilon$ is the emissivity. A Gaussian model [28] is used for $q_{\text{beam}}$:

$$q_{\text{beam}}(\boldsymbol{x}, t) = \frac{2\eta_{\text{beam}} P_{\text{beam}}}{\pi R_{\text{beam}}^2} \exp\left(-2\frac{\|\boldsymbol{x} - \boldsymbol{x}_{\text{beam}}(t)\|^2}{R_{\text{beam}}^2}\right) \tag{4}$$

Where $P_{\text{beam}}$ is the laser beam power, $\eta_{\text{beam}}$ is the absorption coefficient, $R_{\text{beam}}$ is the beam radius, $\boldsymbol{x}_{\text{beam}}(t)$ is the moving heat source location and $\boldsymbol{x}$ is the material point of interest.

In addition, the gas flow increases significantly $H$ for all layers under the flow (see figure 1). This aspect has been modeled in a simplified way, as detailed in section 3.

### *2.2. Assumptions, limitations and strategy*

The equation set (1) to (3) is difficult to solve analytically, mostly because of geometrical complexity and the fact that the domain is time-dependent. We neglect heat fluxes along the tangent direction of the path $\chi$ to overcome this difficulty. Therefore, successive points on $\chi$ can be considered as independent. The validity of this assumption is questionable in the vicinity of the melt pool where temperature gradients are very significant in all directions, especially in the direction of the laser movement. Although the proposed assumption introduce a bias near the melt pool, since the laser is moving at relatively high speed, the effect of heat fluxes along the tangent direction is expected to be limited as the laser moves faster than the heat can diffuse. Moreover, in the rest of the part, heat fluxes along the vertical direction prevail.

This assumption leads to discretize the path $\chi$ in $N_\chi$ positions, and to consider independent computations for each position. The computation points are indexed by $p$ ($1 \leq p \leq N_\chi$), and consist of multilayer composites in the $(r, z)$ plane, where $r$ is the radial coordinate (thickness direction) and $z$ the vertical coordinate. Thus, the assumption leads to consider axi-symmetric multilayer cylinders. However, more complex geometries than cylinders can be approached by combining successive computations with different radii. The core problem relies on a 2D problem, but pseudo-3D temperature fields can be reconstructed by combining several 2D solutions.

The number of layers gradually increases as metal deposition goes on, and $N$ denotes the final number of layers. Each computation point $p$ is characterized by the radius of curvature, and the different times when metal is deposited (denoted by $(t_1^p, \cdots, t_{N+1}^p)$). Thus, different

geometries, laser paths and dwell times can be simulated through different radii of curvature, laser speeds and deposition times.

The simulation strategy consists in approximating the equation set (1) to (3) for each computation point on each time interval $\left[t_n^p, t_{n+1}^p\right]$ ($1 \leq n \leq N$). Thus, each computation point requires $N$ sub-computations. The initial condition on the time interval $\left[t_n^p, t_{n+1}^p\right]$ is simply obtained from the final condition on the previous time interval $\left[t_{n-1}^p, t_n^p\right]$. The proposed strategy is presented in figure 2. In the following, the superscript $p$ is discarded for the sake of clarity.

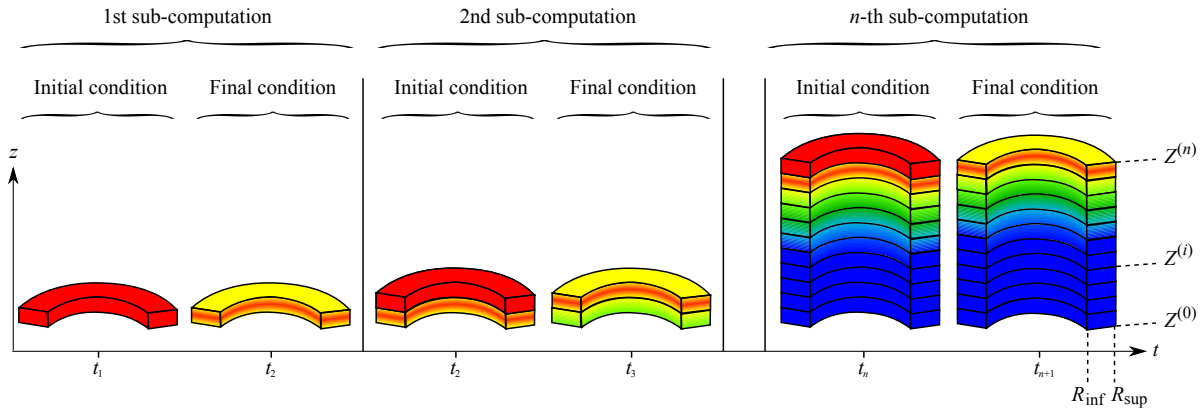


Figure 2: Numerical strategy for each computation point

Although pseudo-3D temperature fields can be computed with the proposed method, there are geometrical restrictions. Indeed, as computation points are independent from each other, boundary conditions (e.g., convection) should not depend on other computation points. Therefore, the proposed method applies to paths $\chi$ that do not intersect themselves (intersection or tangent points). This geometrical restriction excludes the possibility of simulating multi-track structures to obtain a bulk material. Moreover, complex geometries cannot be computed accurately near the intersection or tangent points. Additional developments would be necessary to adapt the proposed strategy to such cases.

Phase proportion rates highly depend on temperature. Therefore, the heat conduction equation (1) is non-linear. This difficulty is overcome by using an alternating algorithm. More precisely, a first estimation of the temperature field is computed by setting the right side term to zero. Then, this estimation is used to update the phase proportion rates and the right side term of (1). On this basis, a new estimation of the temperature field is computed. This procedure is repeated until convergence. Therefore, the non-linear problem is solved as a succession of linear problems.

## 3. Semi-analytical solution for the temperature

This section deals with the derivation of the semi-analytical solution of the heat conduction problem (1) to (3). Because of the alternating algorithm, the volumetric heat $Q^{(i)}$ is assumed to be known in this section. A simple phase transition model is detailed in section 4 to update $Q^{(i)}$. The mathematical solution is derived for the $n$-th sub-computation ($1 \leq n \leq N$) on the

time interval $[t_n, t_{n+1}]$ (see figure 2). Thus, there are $n$ layers defined by:

$$(r, z) \in \left[R_{\text{inf}}, R_{\text{sup}}\right] \times \bigcup_{i=1}^{n} \left[Z^{(i-1)}, Z^{(i)}\right] \tag{5}$$

Where $(i)$ denotes the layer index ($1 \leq i \leq n$), $R_{\text{inf}}$ is the internal radius, $R_{\text{sup}}$ is the external radius, $h_r = R_{\text{sup}} - R_{\text{inf}}$ is the layer thickness, $Z^{(i)}$ are the interfaces positions, and $h_z = Z^{(i)} - Z^{(i-1)}$ is the layer height. The proposed approach requires constant material parameters on the interval $[t_n, t_{n+1}]$. If material parameters depend on temperature, the thermal conductivity $\lambda^{(i)}$ and the thermal diffusivity $D^{(i)}$ can be updated at the end of the time interval.

The derivation of the semi-analytical solution relies on Fourier-Bessel series expansions, interpolation of the volumetric heat by exponential fitting, and orthogonal projection on a finite-dimensional vector space. Mathematical developments are rather technical and are detailed in Appendix A.

### *3.1. Heat sources, initial condition and boundary conditions*

The loss of heat due to radiation and the heat flux applied by the laser are modeled as powers per unit volume instead of powers per unit area. Moreover, the gas flow increases significantly the heat transfer coefficient for all layers under the flow. However, the following mathematical solution is based on a constant heat transfer coefficient. This difficulty is overcome by introducing a negative power per unit volume to model the loss of heat due to the gas flow. Thus, the heat conduction equation (1) reads:

$$\frac{\partial^2 T^{(i)}}{\partial r^2} + \frac{1}{r}\frac{\partial T^{(i)}}{\partial r} + \frac{\partial^2 T^{(i)}}{\partial z^2} - \frac{1}{D^{(i)}}\frac{\partial T^{(i)}}{\partial t} = -\frac{Q^{(i)}(t)}{\lambda^{(i)}} \tag{6}$$

Where $T^{(i)}$ is the temperature, and:

$$Q^{(i)}(t) = \sum_{\phi=1}^{N_\phi} \Delta H_\phi \dot{X}_\phi^{(i)} - \frac{2\sigma\epsilon}{h_r}\left(\left[T^{(i)}\right]^4 - T_{\text{ext}}^4\right) + Q_{\text{beam}}^{(i)}(t) - Q_{\text{gas}}^{(i)}(t) \tag{7}$$

Where the factor $2/h_r$ has been introduced in the radiative term to convert the power at the inner and outer surfaces into a power per unit volume. In addition, $Q_{\text{beam}}^{(i)}$ is the volumetric heat due to the laser. The Gaussian model (4) gives:

$$Q_{\text{beam}}^{(i)}(t) = \begin{cases} \dfrac{2\eta_{\text{beam}} P_{\text{beam}}}{\pi h_z R_{\text{beam}}^2} \exp\left(-2V_{\text{beam}}^2 \dfrac{(t-t_n)^2}{R_{\text{beam}}^2}\right) & i = n-1 \\ 0 & \text{otherwise} \end{cases} \tag{8}$$

Where $V_{\text{beam}}$ is the laser speed. Furthermore, the power per unit volume associated to the gas flow $Q_{\text{gas}}^{(i)}(t)$ corresponds to a convection condition (i.e., $H(T^{(i)} - T_{\text{ext}})$). The heat transfer coefficient associated to the gas flow is approximated with Gaussian function similar to (8), which depends on the laser speed. Therefore $Q_{\text{gas}}^{(i)}(t)$ reads:

$$Q_{\text{gas}}^{(i)}(t) = 2\frac{H_{\text{gas}}}{h_r}(T^{(i)} - T_{\text{ext}}) \exp\left(-2V_{\text{beam}}^2 \frac{(t-t_n)^2}{R_{\text{gas}}^2}\right) \tag{9}$$

Where $H_{\text{gas}}$ is the maximum heat transfer coefficient associated to the gas flow, and $R_{\text{gas}}$ characterizes the area affected by the gas flow. It should be noted that $Q_{\text{gas}}^{(i)}$ depends on $T^{(i)}$ in

(9). Thus, $Q_{\text{gas}}^{(i)}$ is computed by using the previous estimation of the temperature field in the alternating algorithm.

The initial condition on the time interval $[t_n, t_{n+1}]$ is simply obtained from the final condition on the previous time interval $[t_{n-1}, t_n]$, which reads:

$$T^{(i)}(r, z, t = t_n) = T_{\text{ini}}^{(i)}(r, z) \tag{10}$$

Where $T_{\text{ini}}^{(i)}$ is obtained from the previous sub-computation.

The build platform is modeled in a simplified way. It is assumed that the build platform temperature $T_{\text{pla},n}$ is constant on the interval $[t_n, t_{n+1}]$. Of course the real build platform temperature $T_{\text{pla}}(t)$ evolves during the time interval $[t_n, t_{n+1}]$, thus:

$$T_{\text{pla},n} = T_{\text{pla}}(t_n) \tag{11}$$

The build platform temperature $T_{\text{pla},n}$ is updated at the end of each sub-computation. Thus, boundary conditions (2) reduce to:

$$\begin{aligned}
(a): &\begin{cases} \widehat{\lambda}\dfrac{\partial T^{(i)}}{\partial r} = H\,(T^{(i)} - T_{\text{ext}}) & r = R_{\text{inf}} \quad (1 \le i \le n) \\ \widehat{\lambda}\dfrac{\partial T^{(i)}}{\partial r} = -H\,(T^{(i)} - T_{\text{ext}}) & r = R_{\text{sup}} \quad (1 \le i \le n) \end{cases} \\
(b): &\begin{cases} \lambda^{(1)}\dfrac{\partial T^{(1)}}{\partial z} = H_{\text{pla}}\,(T^{(1)} - T_{\text{pla},n}) & z = Z^{(0)} \\ \lambda^{(n)}\dfrac{\partial T^{(n)}}{\partial z} = -H\,(T^{(n)} - T_{\text{ext}}) & z = Z^{(n)} \end{cases} \\
(c): &\begin{cases} T^{(i)} = T^{(i+1)} & z = Z^{(i)} \quad (1 \le i \le n-1) \\ \lambda^{(i)}\dfrac{\partial T^{(i)}}{\partial z} = \lambda^{(i+1)}\dfrac{\partial T^{(i+1)}}{\partial z} & z = Z^{(i)} \quad (1 \le i \le n-1) \end{cases}
\end{aligned} \tag{12}$$

Where the heat transfer coefficient between the build platform and the multilayer structure is denoted by $H_{\text{pla}}$. The loss of heat due to convection corresponds to the conditions $(a)$ and $(b)$, and the continuity of both temperature and heat flux at the interfaces corresponds to the condition $(c)$. Moreover, for the sake of simplicity, the condition $(a)$ is verified in a weak sense. Indeed, the thermal conductivities $\lambda^{(i)}$ $(1 \le i \le n)$ have been replaced by their average denoted by $\widehat{\lambda}$.

### *3.2. Build platform temperature*

The build platform temperature is updated at the end of the $n$-th sub-computation according to the energy received during the time interval. The build platform temperature update reads:

$$\Delta T_{\text{pla}} = T_{\text{pla}}(t_{n+1}) - T_{\text{pla}}(t_n) \tag{13}$$

The heat equation for the build platform reads:

$$\rho_{\text{pla}}\, c_{\text{pla}}\, \frac{\mathrm{d}T_{\text{pla}}}{\mathrm{d}t}(t) = \frac{q_{\text{pla}}(t)}{h_{\text{pla}}} \tag{14}$$

Where $T_{\text{pla}}(t)$ is the time dependent build platform temperature, $h_{\text{pla}}$ is the thickness, $\rho_{\text{pla}}$ is the density and $c_{\text{pla}}$ is the specific heat capacity. In addition, $q_{\text{pla}}$ is the power per unit area received by the build platform, which reads:

$$q_{\text{pla}}(t) = H_{\text{pla}}\left(T_a^{(1)}(t) - T_{\text{pla}}(t)\right) + \widetilde{H}_{\text{pla}}\,(\widetilde{T}_{\text{pla}}(t) - T_{\text{pla}}(t)) \tag{15}$$

Where $T_a^{(1)}(t)$ is the average temperature at the interface between the first layer and the build platform:

$$T_a^{(1)}(t) = \frac{2}{R_{\text{sup}}^2 - R_{\text{inf}}^2} \int_{R_{\text{inf}}}^{R_{\text{sup}}} T^{(1)}(r, Z^{(0)}, t) r \mathrm{d}r \tag{16}$$

And where $\widetilde{H}_{\text{pla}}$ is the heat transfer coefficient between the build platform and the platen underneath. The temperature of the platen is denoted by $\widetilde{T}_{\text{pla}}(t)$, which slowly evolves during the process following the heat equation:

$$\frac{\mathrm{d}\widetilde{T}_{\text{pla}}}{\mathrm{d}t}(t) = \frac{\widetilde{q}_{\text{pla}}(t)}{\widetilde{I}_{\text{pla}}} \tag{17}$$

Where $\widetilde{I}_{\text{pla}}$ is the equivalent thermal inertia ($\text{J.m}^{-2}.\text{K}^{-1}$) of the platen . In addition, $\widetilde{q}_{\text{pla}}$ is the power per unit surface received by the platen and reads:

$$\widetilde{q}_{\text{pla}}(t) = \widetilde{H}_{\text{pla}} \left( T_{\text{pla}}(t) - \widetilde{T}_{\text{pla}}(t) \right) - \widetilde{H}_{\text{pla}} \left( \widetilde{T}_{\text{pla}}(t) - T_{\text{ref}} \right) \tag{18}$$

Where $T_{\text{ref}}$ is a constant temperature. Practically, the coupled system eqs. (14), (15), (17) and (18) is solved numerically by a simple explicit scheme.

### *3.3. Computation times*

Since a semi-analytical solution is proposed, a relatively fast simulation tool is obtained. The computation cost can be analyzed as follows. The semi-analytical solution relies on the computation of eigenvalues defined as the successive roots of a characteristic function (see Appendix A). Roots are computed in advance and stored in a file. In addition, the semi-analytical solution also relies on the determination of several coefficients, which necessitates to inverse a large number of 2×2 matrices and to compute scalar products analytically. However, the computation cost is mostly due to data manipulation aiming at computing series expansions (see Appendix A). Indeed, although the analytical solution is valid continuously (i.e., without time and space discretization), in practice the solution is calculated at different times and positions in each layer. For instance, the computation cost is around 20 minutes with a personal computer (7-cores processor running at 2.7 GHz) for 100 layers with 50 time steps for each cycle and 9 positions in each layer (3 positions along the radial and vertical coordinates respectively). The computation time is only 5 minutes if the solution is extracted only at the center of each layer. It should be noted that the proposed model has been implemented in Scilab [43]. Shorter computation times would likely be obtained with a compiled language such as C.

## 4. Simple model of phase transitions

This section deals with the determination of phase proportion rates, considering a known temperature field. The following approach is adapted to steels. However, similar equations can be derived for other alloys. Very common materials used for LMPDED (e.g., stainless steel 316L) are mostly austenitic. However, a multiphase framework is presented to include high strength steels (see figure 3). Thus, the model enables to determine whether complex multiphase microstructures could be controllably obtained during LMPDED.

Phase proportions are denoted by $X_\phi$ in (1). However, for the sake of clarity, more explicit notations are introduced in figure 3. Phase proportions of liquid, austenite, ferrite, pearlite,

bainite and martensite are respectively denoted by $X_{\text{liq}}, X_{\text{aus}}, X_{\text{fer}}, X_{\text{per}}, X_{\text{bai}}$ and $X_{\text{mar}}$. In addition, each phase transition occurs in a specific temperature range, as shown in figure 3. The liquidus and solidus temperatures are denoted by $T_{\text{liq}}$ and $T_{\text{sol}}$ respectively, and temperatures between which solid state phase transitions occur are denoted by $AE_3$, $AE_1$, BS and MS, and the austenitization temperature is denoted by $T_{\text{aus}}$. The temperatures considered in this paper are listed in table 5. Two different equations are used to model the different phase transitions: the Johnson-Mehl-Avrami-Kolmogorov (JMAK) equation [44–47] and the Koistinen-Marburger (KM) equation [48]. Diffusive phase transitions (i.e., austenite to ferrite, pearlite and bainite) are classically modeled with the JMAK equation, and the displacive phase transition (i.e., austenite to martensite) is classically modeled with the KM equation. Moreover, for the sake of simplicity, solidification and austenitization are both modeled with a KM type equation. Two coefficients $k_\phi$ and $n_\phi$ arise in both the JMAK equation and the KM type equation, where $\phi$ refers to the considered phase transition. The coefficients $(k_\phi, n_\phi)$ considered in this paper are listed in table 6.

More precisely, the equations associated to each phase transition are detailed in the following. Solidification kinetics have been obtained in [28] for the stainless steel 316L. The following KM type interpolation function is used:

$$\begin{cases} \forall T \in \left[T_{\text{sol}}, T_{\text{liq}}\right] \\ X_{\text{aus}} = 1 - \exp\left(-k_{\text{liq}}\left(T_{\text{liq}} - T\right)^{n_{\text{liq}}}\right) \end{cases} \tag{19}$$

Phase transitions driven by carbon diffusion are slow. Thus, typical cooling rates in LMPDED are generally not compatible with the formation of ferrite, pearlite and bainite. However, these phases may be obtained by controlling the build platform temperature and tuning the process parameters. Phase proportions $X_\phi$ (where $\phi$ stands for fer, per or bai) are initially set to zero. The phase proportion variation $\Delta X_\phi$ is computed according to the Johnson-Mehl-Avrami-Kolmogorov (JMAK) equation:

$$\Delta X_\phi = X_{\text{aus}}\left[1 - \exp\left(-k_\phi\left(t - t_\phi\right)^{n_\phi}\right)\right] \tag{20}$$

Where $t_\phi$ is the initial time when the temperature range of the phase transition is reached. Moreover, the phase proportion of martensite is updated according to the KM equation:

$$\begin{cases} \forall T \leq \text{MS} \\ \Delta X_{\text{mar}} = X_{\text{aus}}\left[1 - \exp\left(k_{\text{mar}}\left(T - \text{MS}\right)^{n_{\text{mar}}}\right)\right] \end{cases} \tag{21}$$

Where $\Delta X_{\text{mar}}$ is the phase proportion variation. Usually, the JMAK equation is used for austenitization, which depends on the heating rate [49, 50]. However, as heating rates are very high during LMPDED, it seems sufficient to use a KM type interpolation similar to (19). Therefore, the phase proportion of austenite is updated as follows during austenitization:

$$\begin{cases} \forall T \in [\text{AE}_3, T_{\text{aus}}] \\ \Delta X_{\text{aus}} = X\left[1 - \exp\left(-k_{\text{aus}}\left(T - AE_3\right)^{n_{\text{aus}}}\right)\right] \\ X = X_{\text{fer}} + X_{\text{per}} + X_{\text{bai}} + X_{\text{mar}} \end{cases} \tag{22}$$

Where $\Delta X_{\text{aus}}$ is the phase proportion variation.

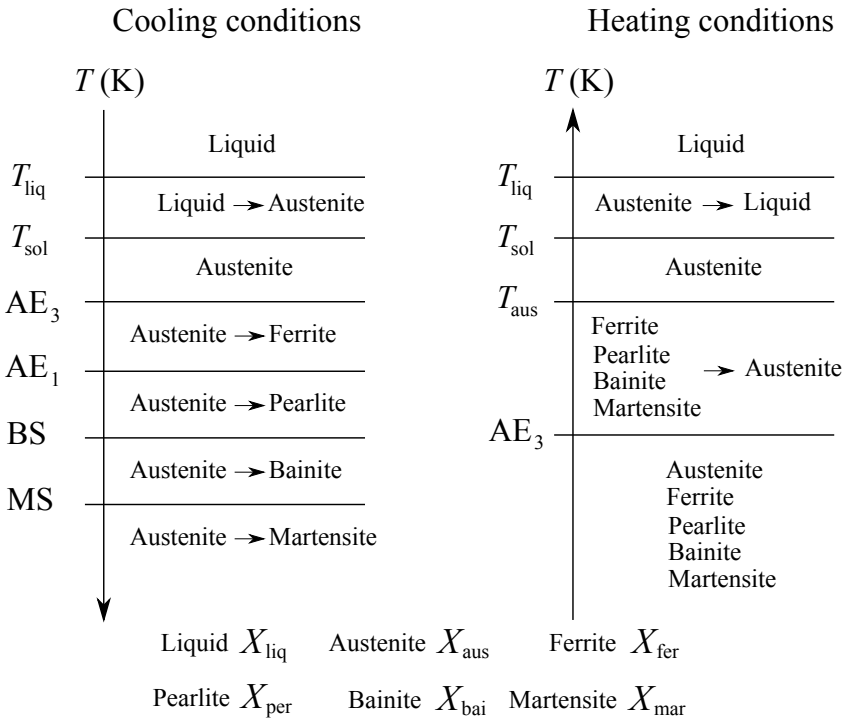


Figure 3: Phase transitions for steel

## 5. In-situ experiments

In this section, the model is compared to in-situ experiments. The chosen material is MetcoClad™ 316L-SI, whose chemical composition is provided in table 1. This grade is similar to AISI Type 316L (UNS S31603); the main difference is the higher content in silicon preventing oxidation.

Table 1: Chemical composition in weight percent

| Fe | Ni | Cr | Mo | Si | Mn | C | Others |
|---|---|---|---|---|---|---|---|
| Balance | 12 | 17 | 2.5 | 2.3 | 1 | 0.03 | ≤0.5 |

The procedure involves fabricating four cylinders of different diameters with a BeAM™ machine. Tests are summarized in table 2. The build platforms are square plates made of 316L. For all tests, the laser path is continuous, and there is no dwell time.

Table 2: Summary of experiments

| Test | Diameter $D$ (mm) | Speed $V_{\text{beam}}$ (mm.s$^{-1}$) | Cycle duration $t_{n+1} - t_n$ (s) | Spot $h_{\text{spot}}$ (mm) | Pyrometer (emissivity) |
|---|---|---|---|---|---|
| 1 | 40 | 33.33 | 3.77 | 10 | IGAR6 ($\epsilon_{\text{IGAR6}} = 0.6$) |
| 2 | 60 | 33.33 | 5.66 | 10 | IGAR6 ($\epsilon_{\text{IGAR6}} = 0.6$) |
| 3 | 100 | 33.33 | 9.42 | 10 | IGAR6 ($\epsilon_{\text{IGAR6}} = 0.6$) |
| 4 | 40 | 30 | 4.19 | 20 | M318 ($\epsilon_{\text{M318}} \simeq 0.65$) |

Temperature measurements are carried out by an infrared laser pyrometer, which enables to record the temperature at a single location. Two different pyrometers have been used for different tests, as listed in table 2. The first pyrometer is a LumaSense™ IGAR6 (spectral range 2.0 - 2.5 μm) with a spot size estimated to around 2 mm. The second pyrometer is a Sensortherm™ M318 (spectral range 1.62 - 2.1 μm) with a spot size estimated to around 1.4 mm. The measured temperature is an average over the zone covered by the spot. The emissivity depends on the material, wavelength range, temperature, roughness, etc. The emissivity of the IGAR6 pyrometer has been calibrated at different temperatures on a part fabricated with the BeAM™ machine. The emissivity is rather constant and fixed to $\epsilon_{\text{IGAR6}} = 0.6$. However, the emissivity has not been calibrated for the M318 pyrometer. Thus, the test 4 is more qualitative. Since the spectral ranges are similar for both pyrometers, it is reasonable to fix the emissivity of the M318 pyrometer to a value similar to that of the IGAR6 pyrometer. An acceptable agreement with the model is obtained for $\epsilon_{\text{M318}} \simeq 0.65$.

Raw data of test 1 are presented in figure 4. Similar results are obtained for the other tests. Four zones are identified. Initially, the pyrometer focuses above the part. Thus, the pyrometer records only erratic reflections on the build plate and the machine nozzle. This zone cannot be interpreted and will be discarded subsequently. The second zone starts when significant temperature peaks are recorded. These temperature peaks indicate that the melt pool reached the spot focused by the pyrometer. However the spot is split between the foreground and the background of the part (see figure 5). Therefore, there are two temperature peaks for each cycle. The third zone starts when the spot fully lies on the foreground of the part, and a single temperature peak is recorded for each cycle. The temperature drift is due to the fact that the heat source is moving increasingly further from the measurement spot. As the temperature decreases, measurements are more affected by uncertainties and errors. Indeed, reflections on the build plate and the machine nozzle are responsible for disturbance in the measurements (see figure 5), which becomes dominant over the temperature. The fourth zone simply corresponds to the fast cooling when the laser is turned off.

All the known parameters (physical constants, material properties extracted from [51] and [28], geometrical parameters and laser properties) are listed in table 3. The other parameters, listed in table 4, have been adjusted so that measurements of test 1 agree well with the model. The comparison is presented in figure 6. The relative error in percentage is presented in figure 7. Large localized discrepancies can be noticed and are mainly due to the limitations of the measurement device. Indeed, the detection on the background for the first cycles introduce errors as well as the saturation of the measured temperature and optical disturbances. Excepted these localized errors, the relative error remains below 7.5% and the average relative error is around 2.6%.

Then, the same set of parameters has been used to simulate the other experimental conditions (test 2 to test 4). Tests 1 to 3 have been performed successively on different build platforms (initially at room temperature), however the temperature of the platen $\widetilde{T}_{\text{pla}}$ slightly increases from one test to another. Thus, the initial platen temperature is taken from the final platen temperature of the previous test. Comparisons between measurements and the proposed model are presented in figures 8, 9 and 10. Good agreement is observed between measurements and numerical results. Some discrepancies can be observed and are likely due to the simplifying assumptions of the model.

In addition, for test 4 a simulation has also been performed by neglecting the heat loss due to the gas flow (i.e., $H_{\text{gas}} = 0$) and compared to the measurements and the complete simulation.

Thus, the effect of the argon flow is evidenced in figure 11. (Results have been shifted to facilitate the comparison). On this basis, it seems that the effect of the gas flow should not be neglected.

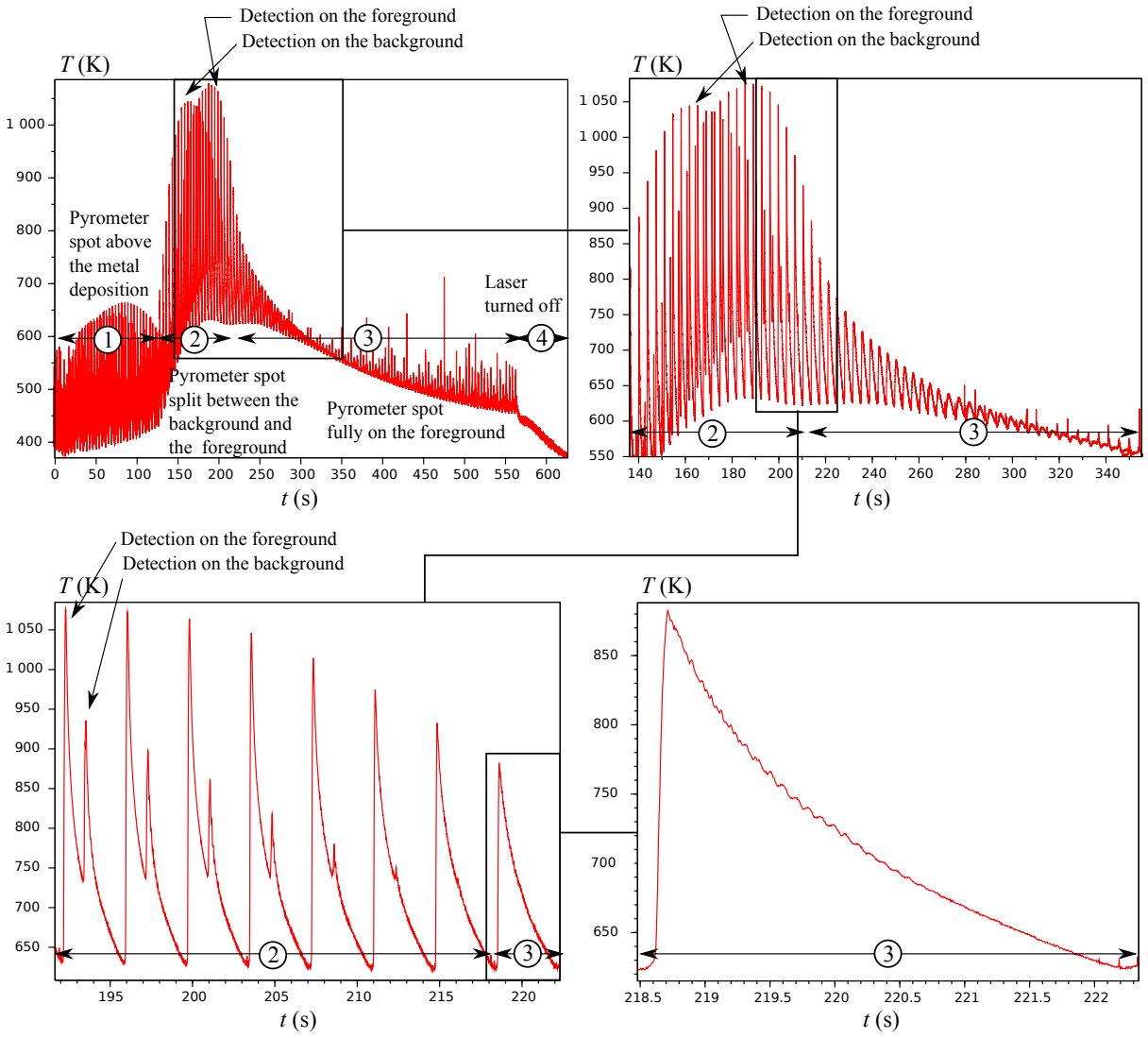


Figure 4: Raw data (test 1)

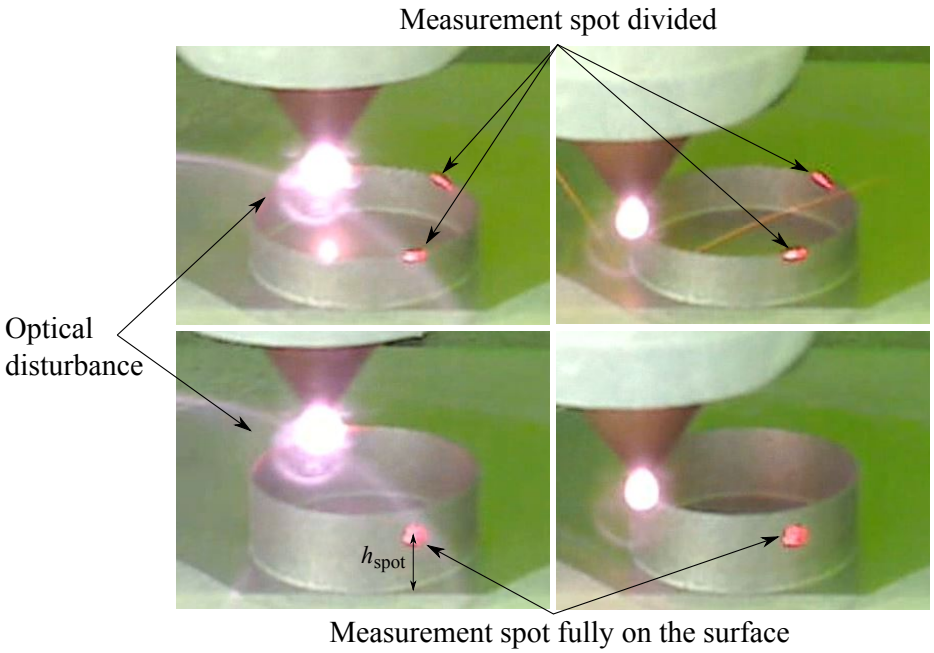


Figure 5: Optical issues during the in-situ experiments (test 1)

Table 3: Known parameters

| | | | |
|---|---|---|---|
| Stefan-Boltzmann constant | $\sigma$ | (W.mm$^{-2}$.K$^{-4}$) | $5.670374 \times 10^{-14}$ |
| Build platform thickness | $h_{\text{pla}}$ | (mm) | 2 |
| Layer height | $h_z$ | (mm) | 0.2 |
| Layer thickness | $h_r$ | (mm) | 0.75 |
| Enthalpy change (solidification) | $\Delta H_{\text{sol}}$ | (J.mm$^{-3}$) | 2.1 |
| Specific heat capacity | $c_p$ | (J.g$^{-1}$.K$^{-1}$) | 0.5 |
| Density | $\rho$ | (g.mm$^{-3}$) | 0.008 |
| Thermal conductivity | $\lambda$ | (W.mm$^{-1}$.K$^{-1}$) | 0.021 |
| Laser beam power | $P_{\text{beam}}$ | (W) | 245 |
| Laser beam radius | $R_{\text{beam}}$ | (mm) | 0.338 |
| External temperature | $T_{\text{ext}}$ | (K) | 300 |
| Initial build platform temperature | $T_{\text{pla}}(0)$ | (K) | 293.15 |
| Initial platen temperature | $\widetilde{T}_{\text{pla}}(0)$ | (K) | 293.15 (test 1 and 4)<br>315 (test 2)<br>331 (test 3) |
| Reference temperature | $T_{\text{ref}}$ | (K) | 293.15 |

Table 4: Parameters identified from test 1

| | | | |
|---|---|---|---|
| HTC air/part | $H$ | ($\mathrm{W.mm^{-2}.K^{-1}}$) | 15 |
| HTC part/build platform | $H_{\mathrm{pla}}$ | ($\mathrm{W.mm^{-2}.K^{-1}}$) | 20000 |
| HTC build platform/platen | $\widetilde{H}_{\mathrm{pla}}$ | ($\mathrm{W.mm^{-2}.K^{-1}}$) | 3000 |
| HTC gas flow/part | $H_{\mathrm{gas}}$ | ($\mathrm{W.mm^{-2}.K^{-1}}$) | 12500 |
| Deposition temperature | $T_{\mathrm{dep}}$ | (K) | 2200 |
| Thermal inertia of the platen | $\widetilde{I}_{\mathrm{pla}}$ | ($\mathrm{J.mm^{-2}.K^{-1}}$) | 6 |
| Absorption coefficient | $\eta_{\mathrm{beam}}$ | (-) | 0.5 |
| Gas flow radius | $R_{\mathrm{gas}}$ | (mm) | 20 |

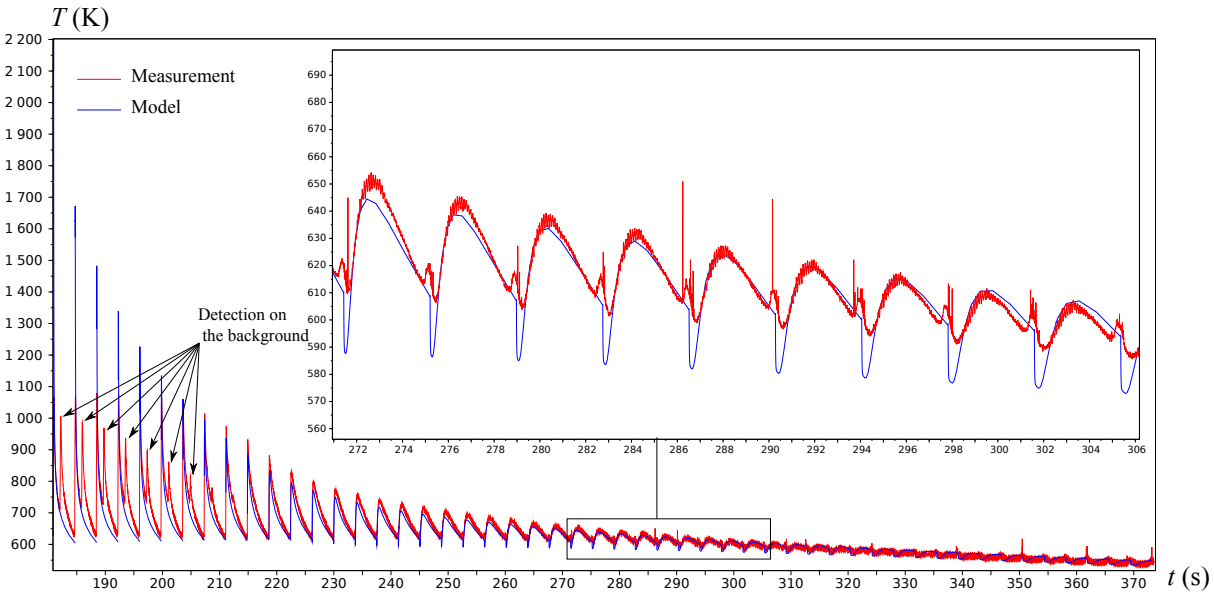


Figure 6: Comparison between measurements and the present model (test 1)

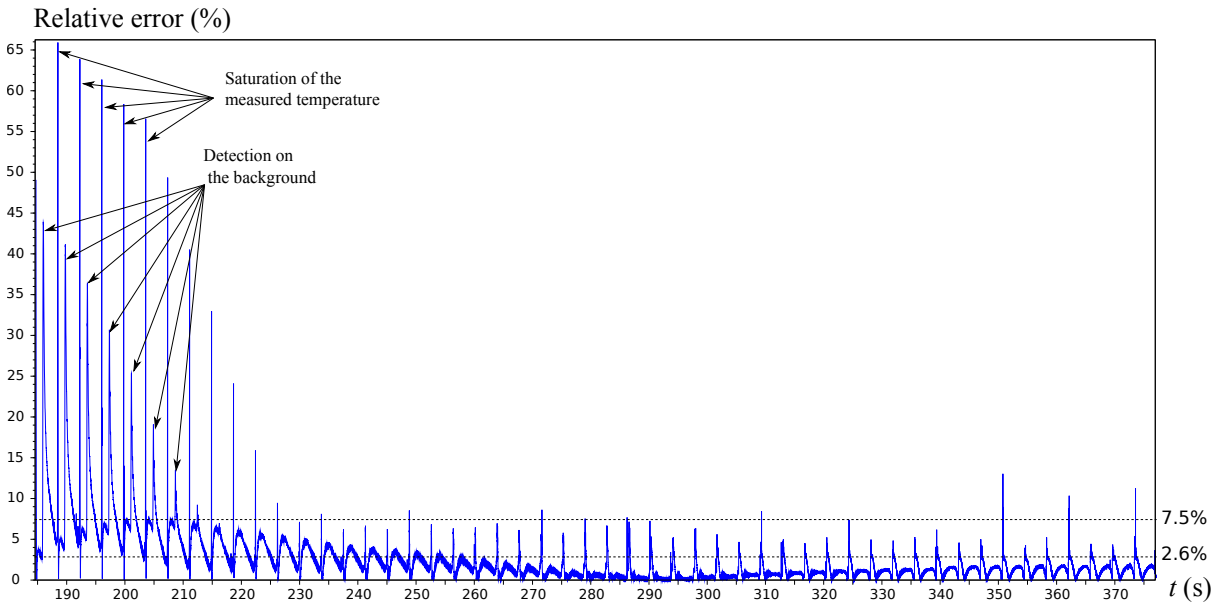


Figure 7: Relative error in % (test 1)

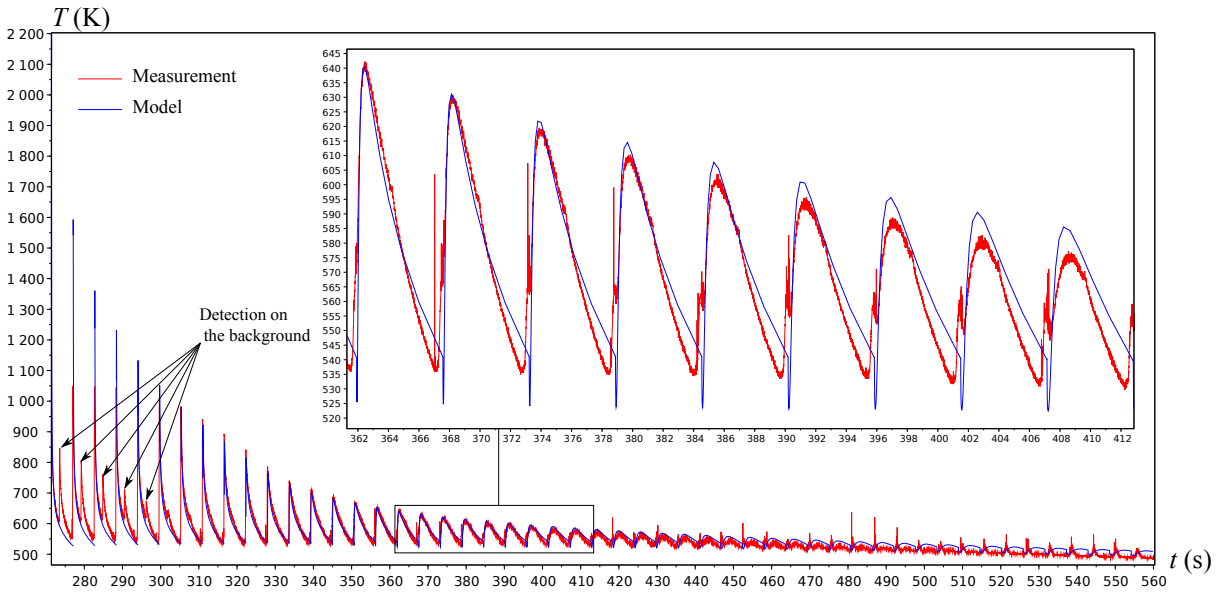


Figure 8: Comparison between measurements and the present model (test 2)

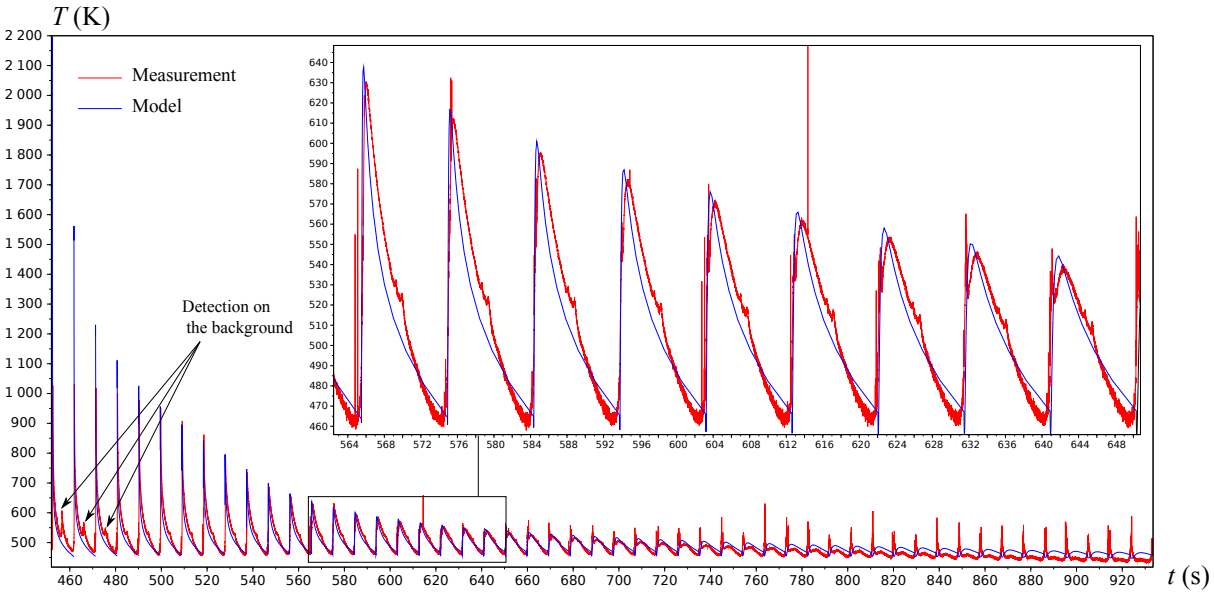


Figure 9: Comparison between measurements and the present model (test 3)

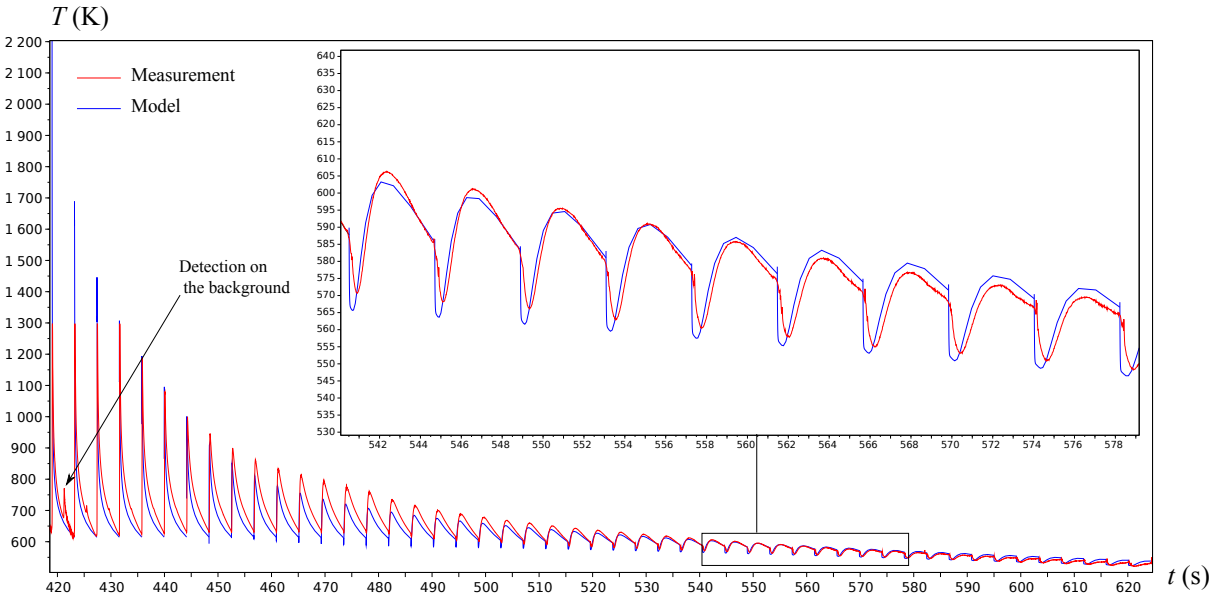


Figure 10: Comparison between measurements and the present model (test 4)

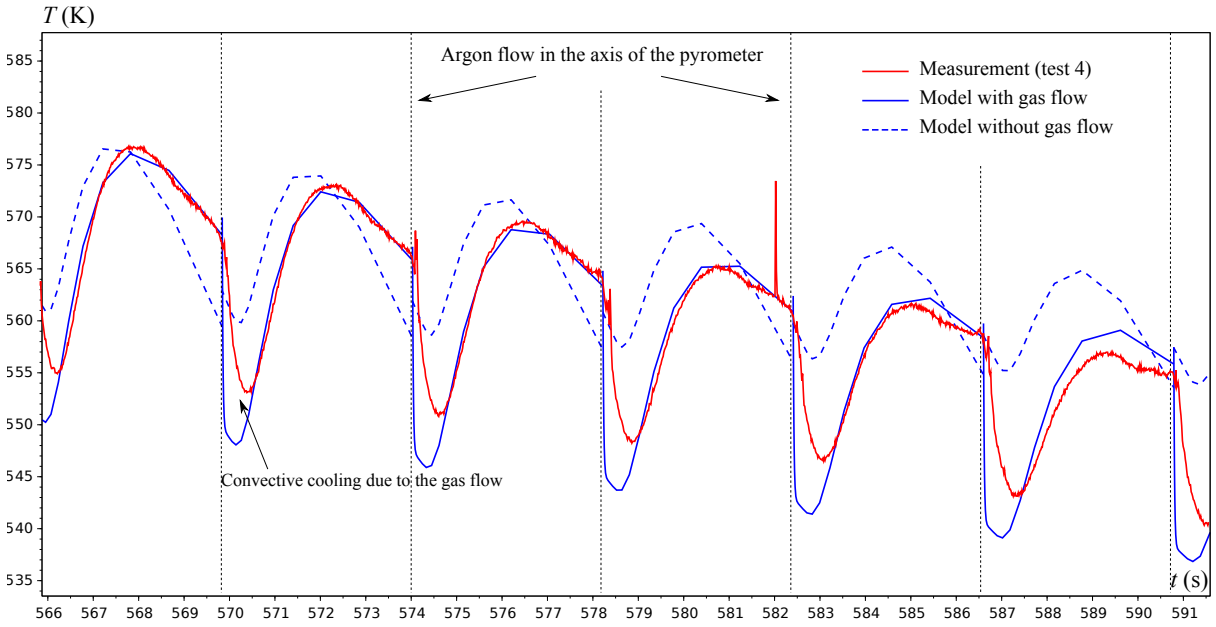


Figure 11: Effect of gas flow

## 6. Influence of process parameters

### *6.1. Reference computation*

In this section, the model is used to demonstrate the influence of some process parameters. This illustrates the design capability of the proposed approach. The material is assumed to be stainless steel 316L, which is essentially austenitic. Thus, solid-state phase transitions are not analyzed in this section. However, multiphase structures are investigated in section 7. In addition, a simple cylindrical structure is analyzed but a more complex geometry is investigated in section 8. A first computation is proposed as a reference for the following comparisons. Simulation parameters are identical to those listed in table 3 and 4 and corresponds to test 1 in table 2. Moreover, all computations consist of 100 layers. Since the laser path is continuous, the time between two depositions does not vary and is $t_{n+1} - t_n = 3.77$ s. The temperature evolution at fixed points on some layers is presented in figure 12. The temperature field is presented at different times in figure 13. The temperature is saturated at 1300 K for the sake of readability. The temperature cycling clearly presents a pseudo-steady-state. The global temperature increases at the beginning and then drifts during the rest of the simulation, which is due to build platform temperature variations. Temperature gradients are computed by finite differences and are presented as a vector field (field of colored arrows) in figure 14 in a zone including the melt pool. The temperature field is also presented with some isotherms in order to identify the melt pool. It is clear that in the vicinity of the melt pool, the assumption consisting in neglecting heat fluxes along the tangent direction is questionable.

In addition, a comparison between the reference computation and a simulation without latent heat (i.e., $\Delta H_{\text{sol}} = 0$) is presented in figure 15 in order to show the effect of phase transitions on temperature. Thus, the coupling between heat conduction and phase transition is not negligible, especially for a large number of layers.

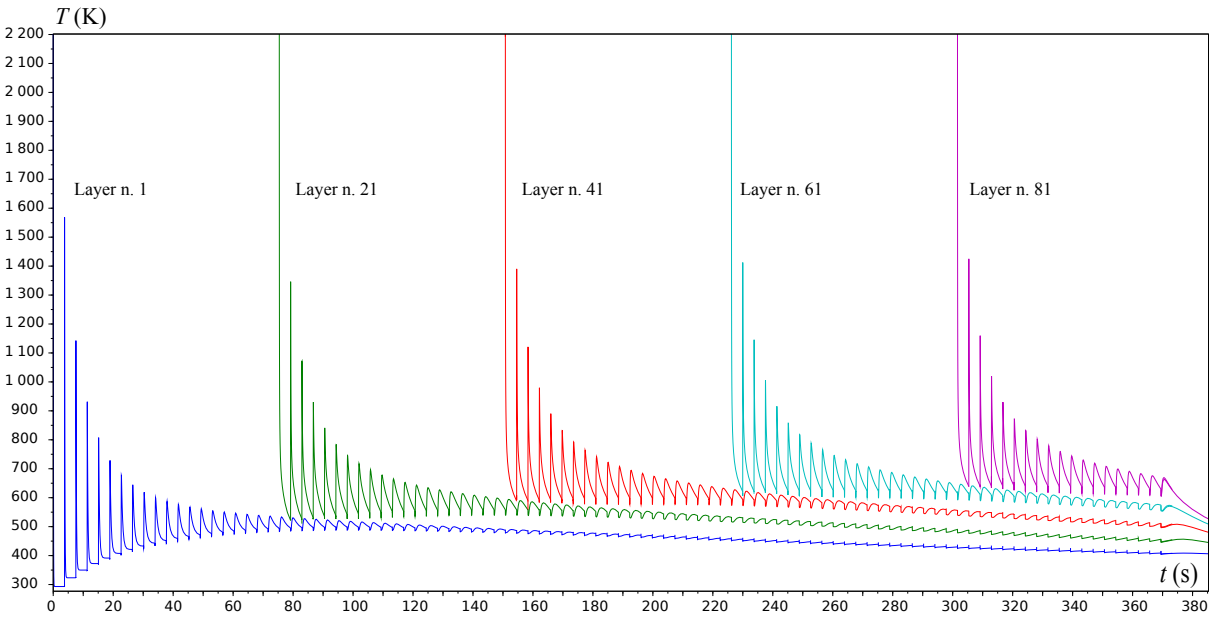


Figure 12: Temperature evolution of some layers for the reference computation

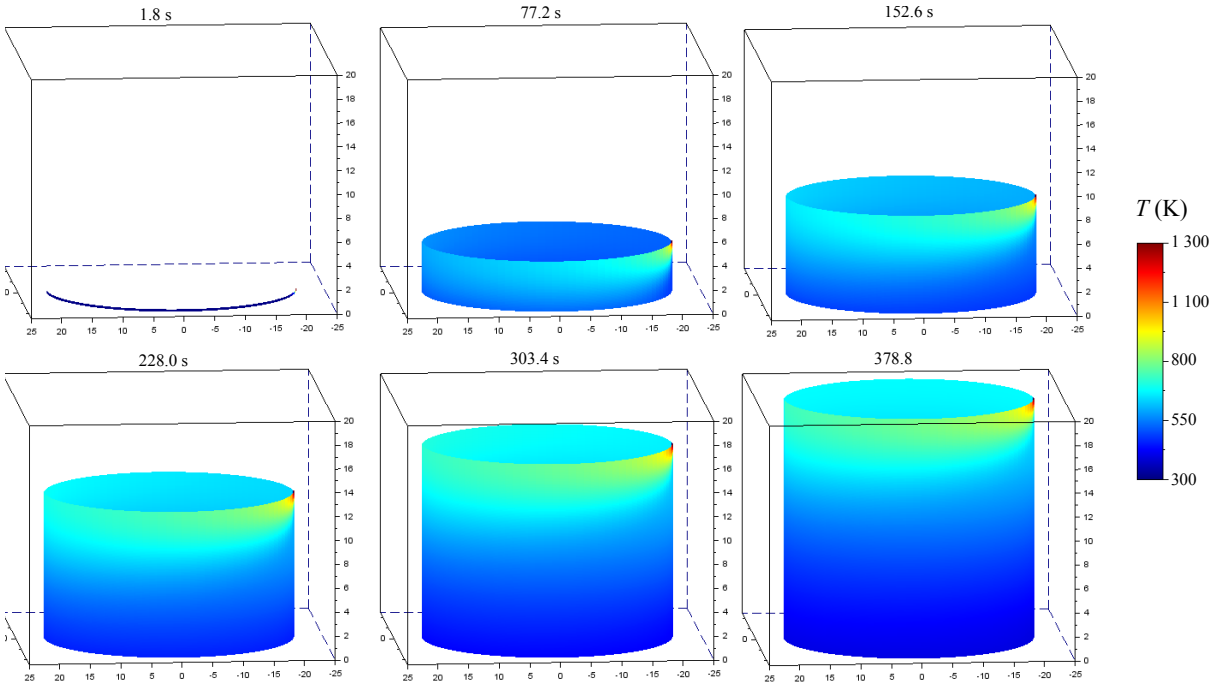


Figure 13: Temperature field of the reference computation

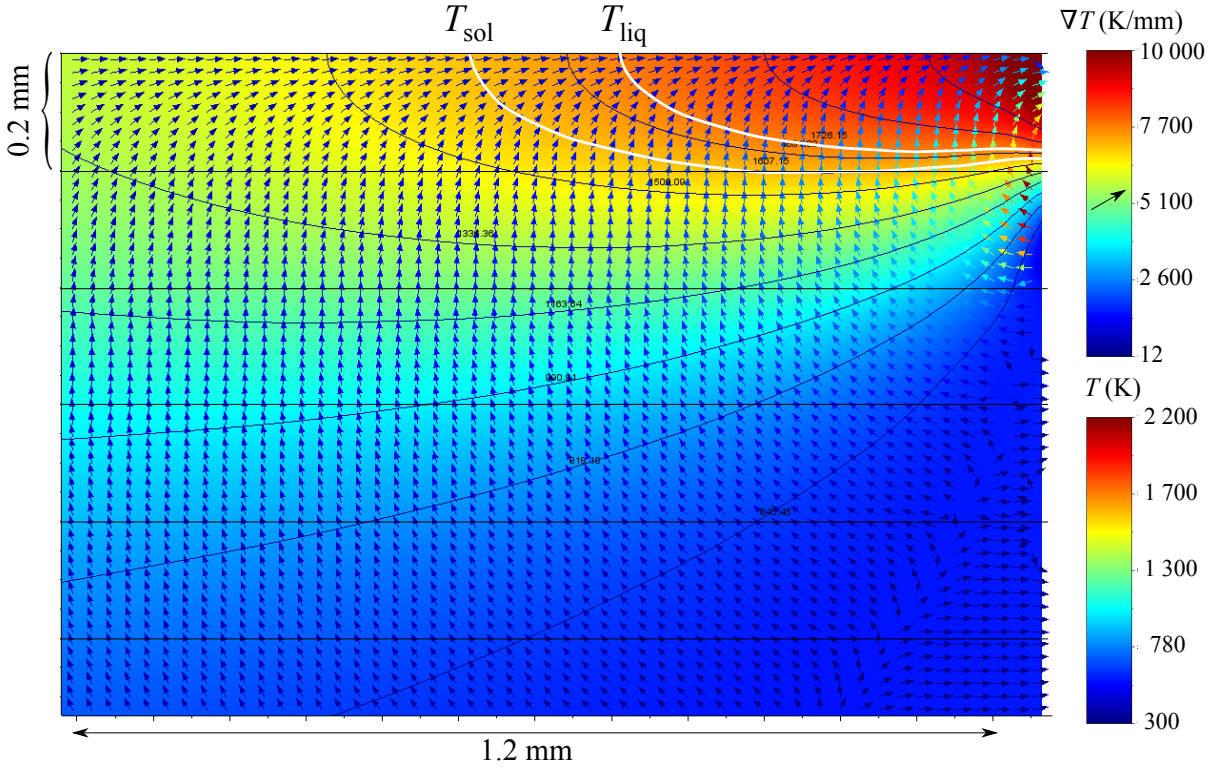


Figure 14: Reference computation: temperature and gradient (vector field) and some isotherms after 40 layers

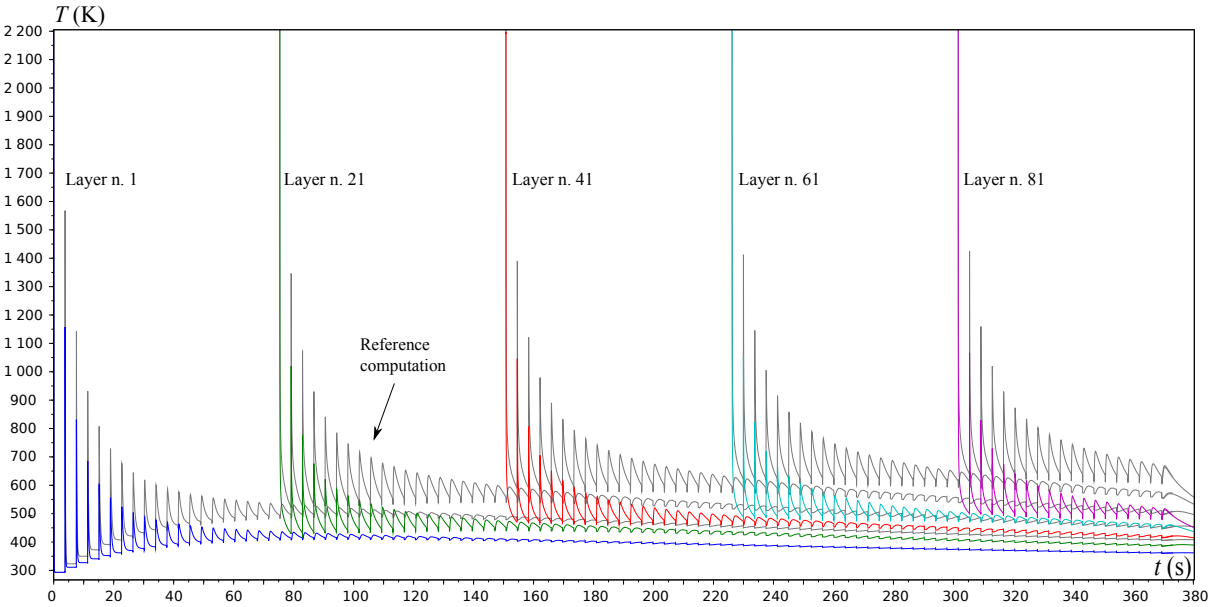


Figure 15: Effect of latent heat

### *6.2. Dwell times*

Simulation parameters are identical to those chosen for the reference computation excepted the dwell time set to 2 s. Results are presented in figure 16 and compared to the reference computation. The temperature field is also presented at different times in figure 17. The main effect is that the build platform temperature increases to a lower value and the part cools down

between each layer. Thus, the metal is deposited on a cooler structure, which locally increases temperature gradients in comparison with the simulation without dwell time as shown in figure 18. In addition, the melt pool size is reduced. Therefore, dwell times may be used to partially control the crystallization pattern and residual stresses due to temperature gradients. Moreover, dwell times have an effect on the direction of crystallization mostly aligned with the temperature gradient [52, 53].

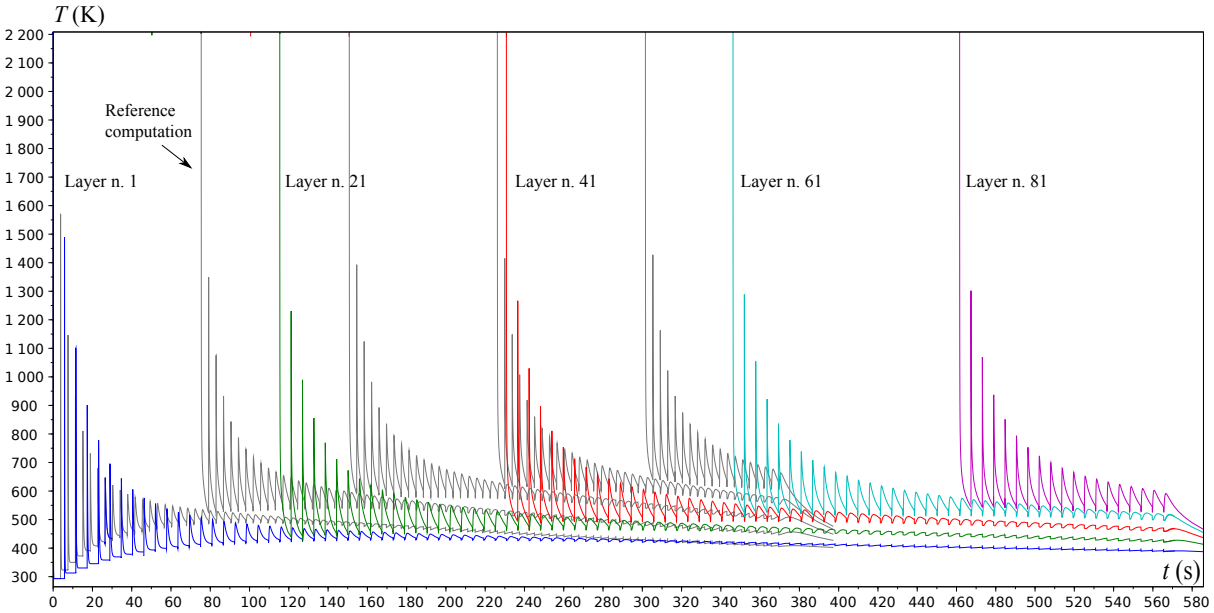


Figure 16: Effect of dwell time: temperature evolution of some layers

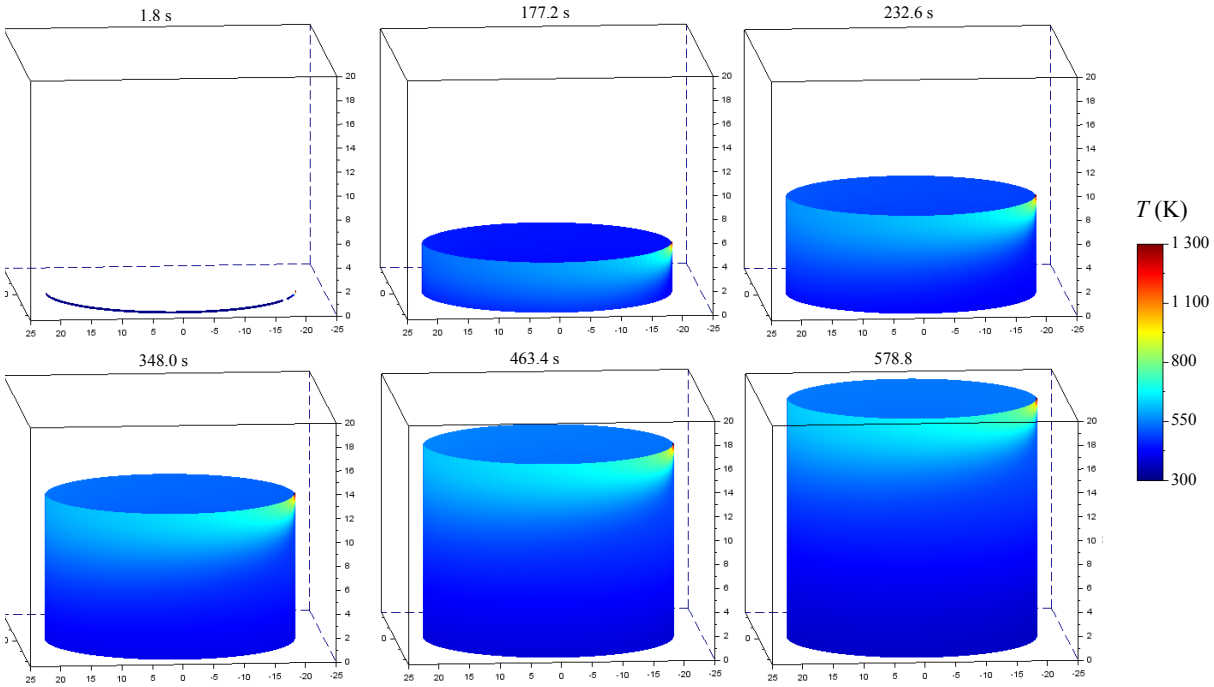


Figure 17: Effect of dwell time: temperature field

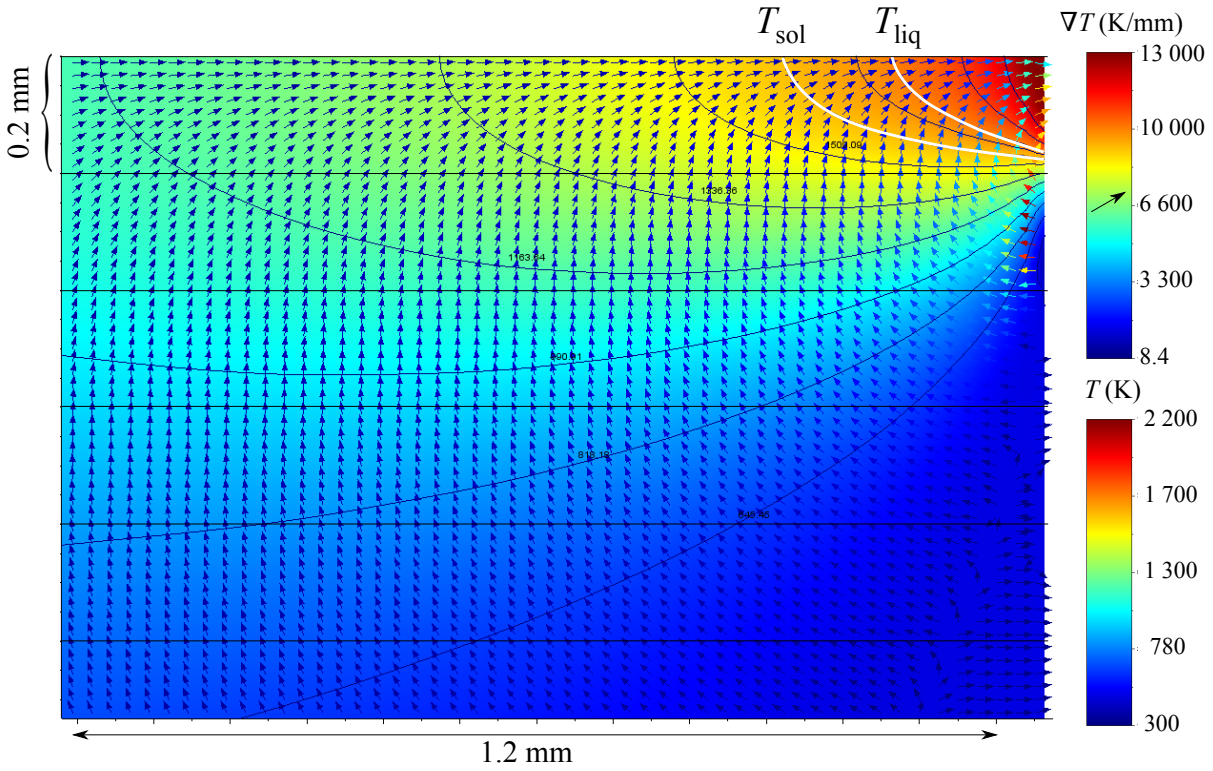


Figure 18: Effect of dwell time: temperature and gradient (vector field) and some isotherms after 40 layers

### *6.3. Laser speed*

Simulation parameters, except the parameter of laser speed set to 50 mm.s$^{-1}$, are identical to those of the reference computation. Results are presented in figure 19 and compared to the reference computation. The temperature field is also presented at different times in figure 20. Increasing the laser speed tends to reach higher temperatures in the part. This can be explained by the fact that the time between two successive metal depositions is shorter ($t_{n+1} - t_n = 2.51$ s) when the laser speed is higher. However, since the laser speed explicitly arises in (8), the energy brought by the laser is lower for higher laser speed. This effect is negligible in comparison to the reduction of the time between two successive metal depositions.

Thus, the laser speed could be used to partially control phase transitions. Indeed, diffusive phase transitions are slow and occur only if the temperature is maintained long enough in the range of the phase transition. To that extent, adjusting the laser speed may contribute to control microstructures. Moreover, local temperature gradients slightly decrease in comparison with the reference computation and the melt pool size increases, as shown in figure 21. Thus, the crystallization pattern is affected by the laser speed.

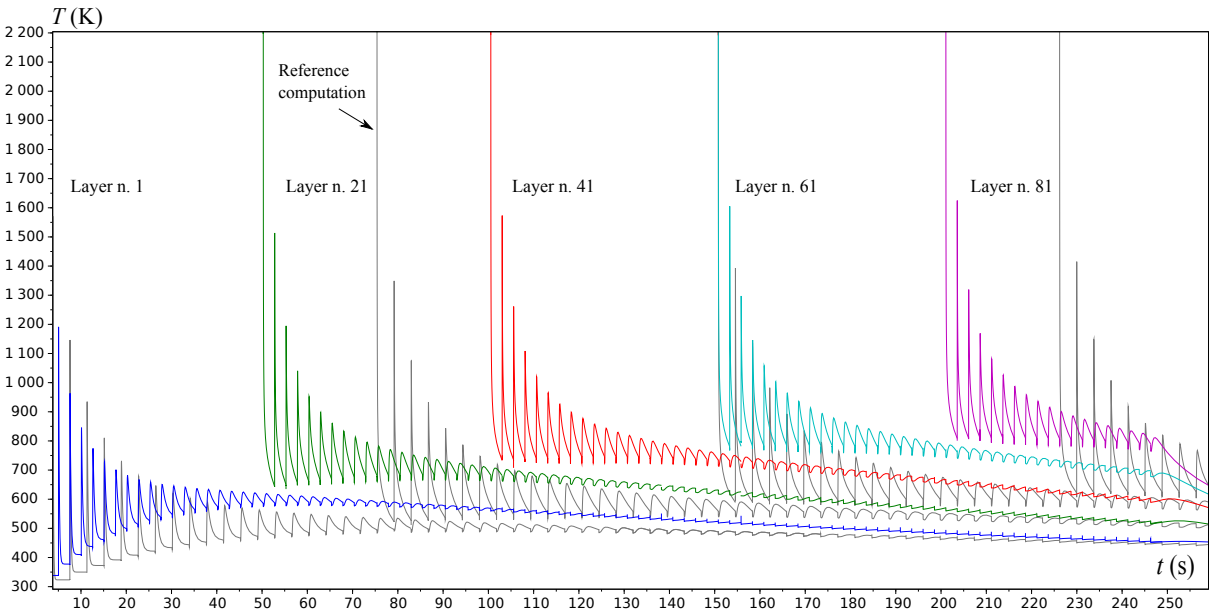


Figure 19: Effect of laser speed: temperature evolution of some layers

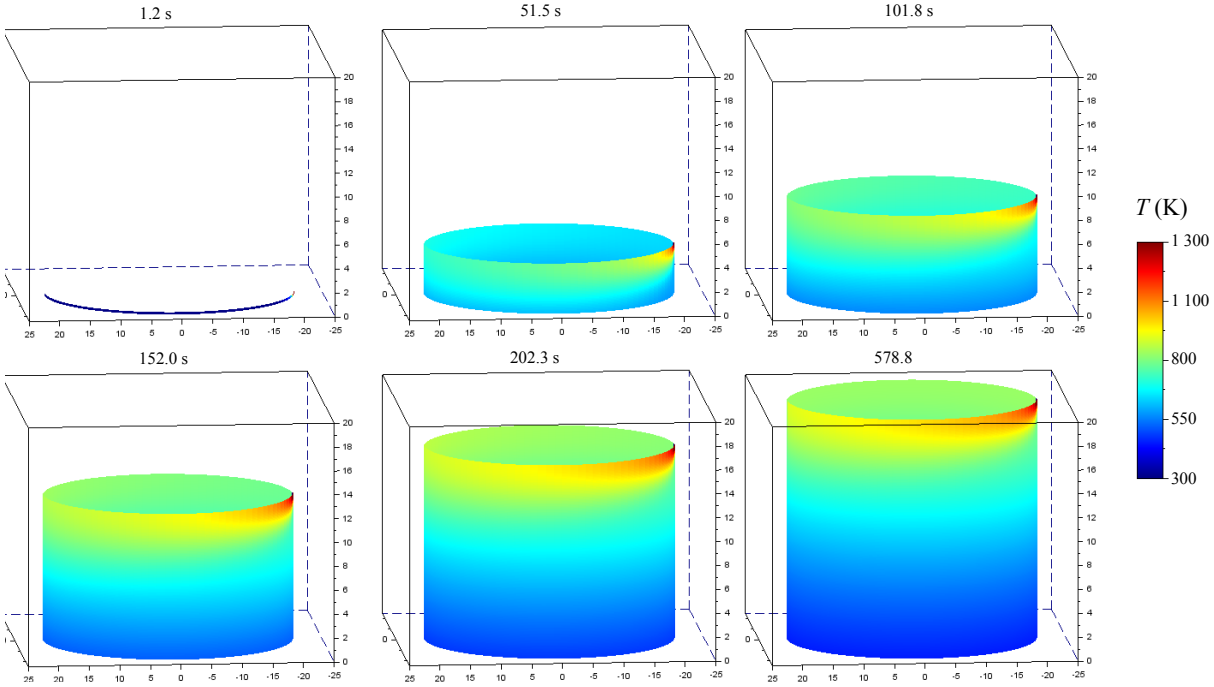


Figure 20: Effect of laser speed: temperature field

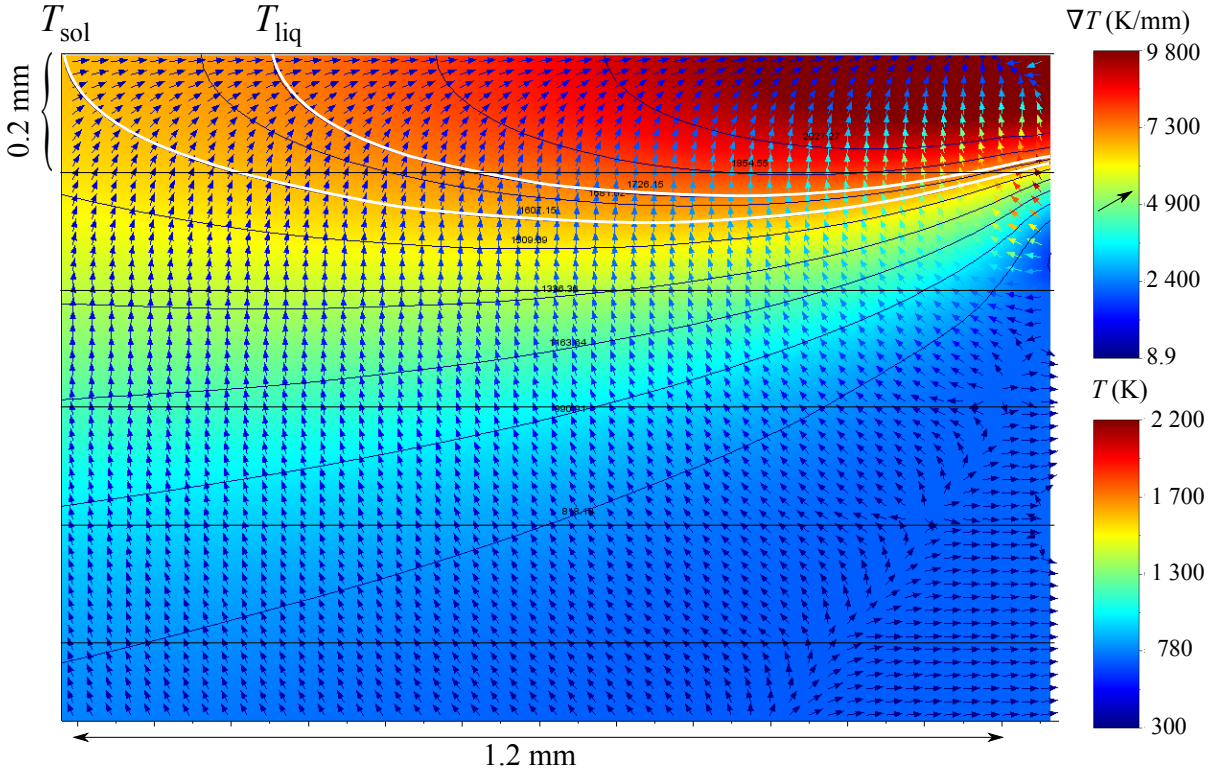


Figure 21: Effect of laser speed: temperature and gradient (vector field) and some isotherms after 40 layers

### *6.4. Laser path*

Simulation parameters are identical to the reference computation. The only difference is that the laser path is changing direction at each cycle. This is modeled by adjusting the time between each metal deposition as detailed in section 2.2. The laser path $\chi$ is discretized as shown in figure 22, and only 9 points have been computed (in red). Between these computation points, the temperature field is approximated by linear interpolation. Temperature cycles are presented for one computation point in figure 23. The general behavior is similar to those presented in figure 12 for the continuous path. However, as the path direction is alternating, each pair of cycles is composed of two cycles of different durations. In addition, the temperature field at different times is presented in figure 24. As expected, the temperature gradient changes direction at each laser pass, leading to microstructures with herringbone patterns [53].

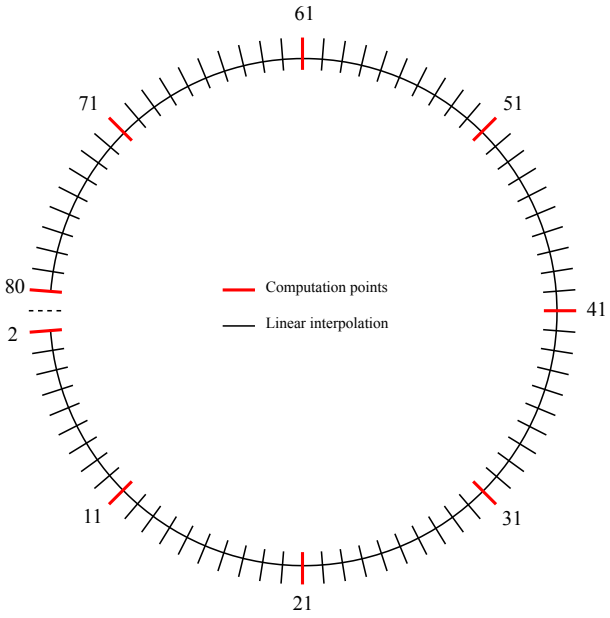


Figure 22: Discretization of the path

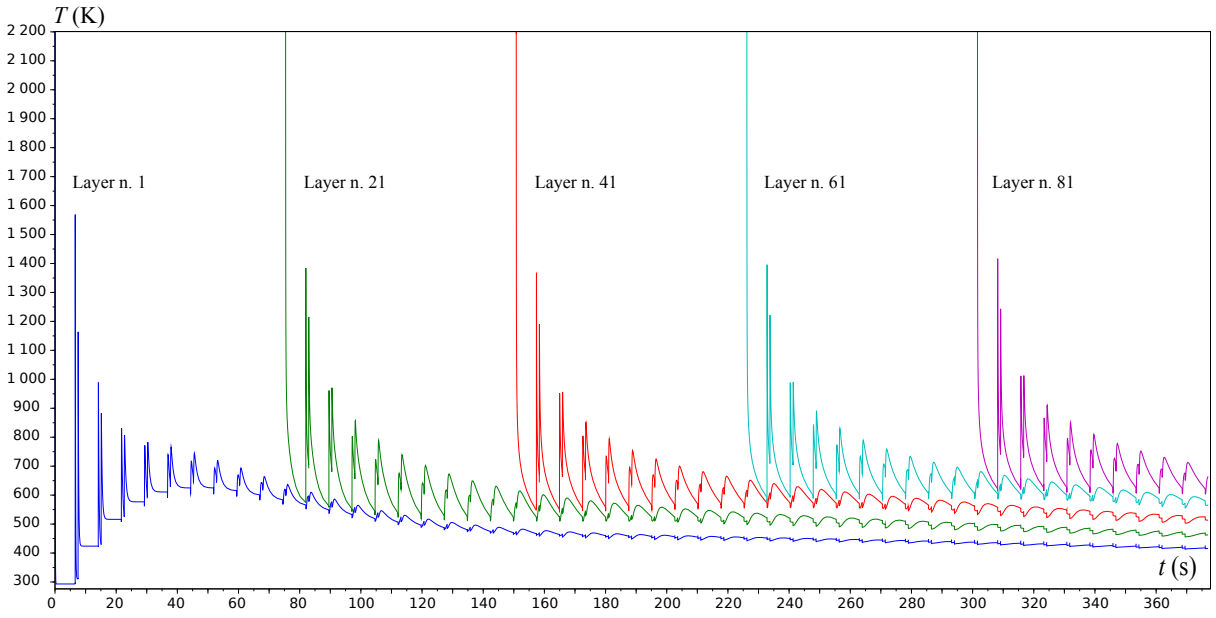


Figure 23: Effect of laser path: temperature evolution of some layers ($\chi_2$)

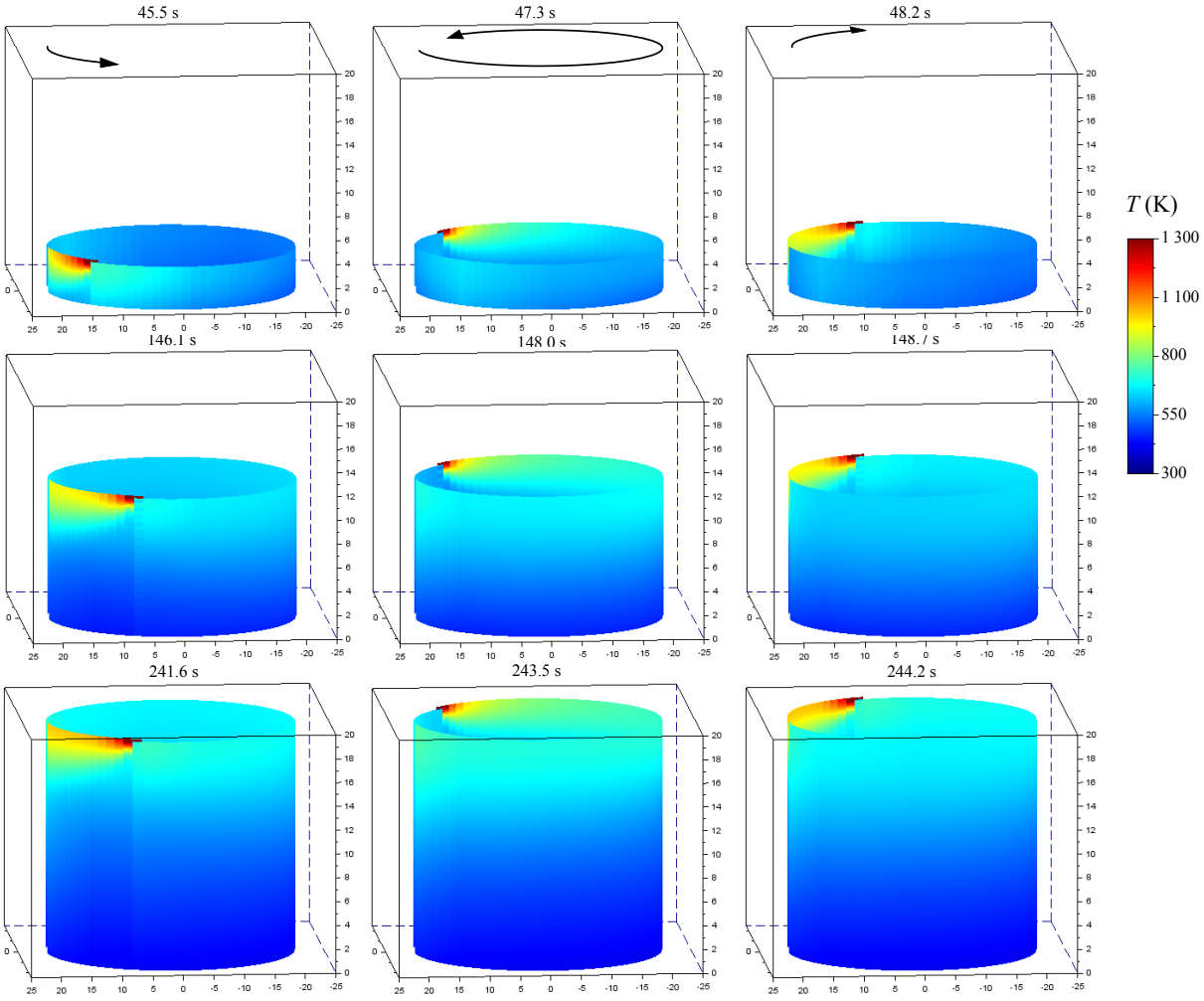


Figure 24: Effect of laser path: temperature field

## 7. Analysis of phase transitions

An austenitic steel has been modeled in the previous section. Multiphase transitions are now considered to show that thermal cycling induces a complex history of phase transitions. Thus, controlling the microstructure for multiphase steels is likely difficult and would necessitate an optimization loop and the addition of temperature control devices (e.g., control of the build platform temperature). The simulation is performed with the same simulation parameters as the reference computation. However, all phase transitions detailed in section 4 are included. Transition temperatures are listed in table 5 and coefficients are listed in table 6.

Table 5: Temperatures between which phase transitions occur

| | | | |
|---|---|---|---|
| Liquidus temperature | $T_{\text{liq}}$ | (K) | 1726.15 |
| Solidus temperature | $T_{\text{sol}}$ | (K) | 1607.15 |
| Temperature end of austenitization | $T_{\text{aus}}$ | (K) | 1125.15 |
| Temperature start of ferrite | $AE_3$ | (K) | 973.15 |
| Temperature start of pearlite | $AE_1$ | (K) | 823.15 |
| Temperature start of bainite | BS | (K) | 713.15 |
| Temperature start of martensite | MS | (K) | 593.15 |

Table 6: Coefficients of the phase transition model

| Coefficient | Liquid | Austenite | Ferrite | Pearlite | Bainite | Martensite |
|---|---|---|---|---|---|---|
| $k$ | 0.02 | 0.000002 | 0.0001 | 0.00015 | 0.00015 | 0.011 |
| $n$ | 1.22 | 3 | 1.5 | 1.5 | 1.5 | 1 |

Results presented in figure 25 demonstrate a complex history. The first cycle presents a rapid solidification followed by a martensitic phase transition. Then, as the temperature increases significantly during the second cycle, a rapid austenitization occurs, followed by a second martensitic phase transition. This process repeats itself during one or two more cycles until the temperature increase is not sufficient to reach the austenitization temperature. The phase proportion field is presented in figure 26. As the part cools down near the build platform, the martensite proportion increases. For the tested condition, ferrite, pearlite and bainite cannot be formed as cooling rates are too high. These phases can only be formed by optimizing process parameters and adding temperature control devices, which necessitates a fast model of the entire process such as the model proposed in this paper.

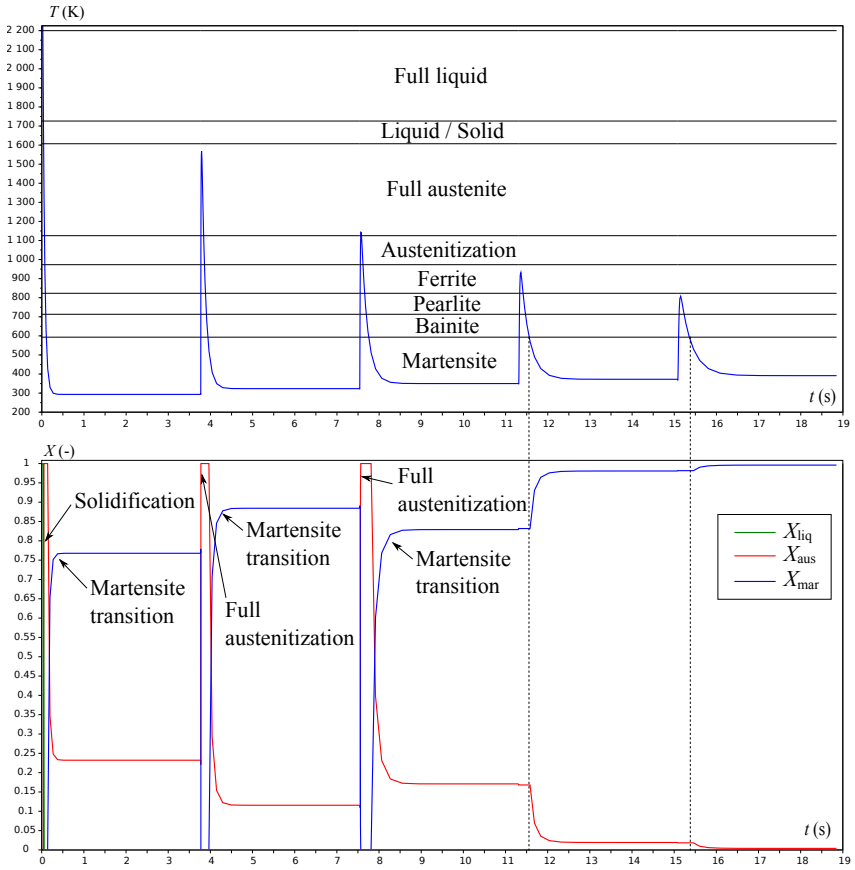


Figure 25: Temperature path and phase transitions for the first layer

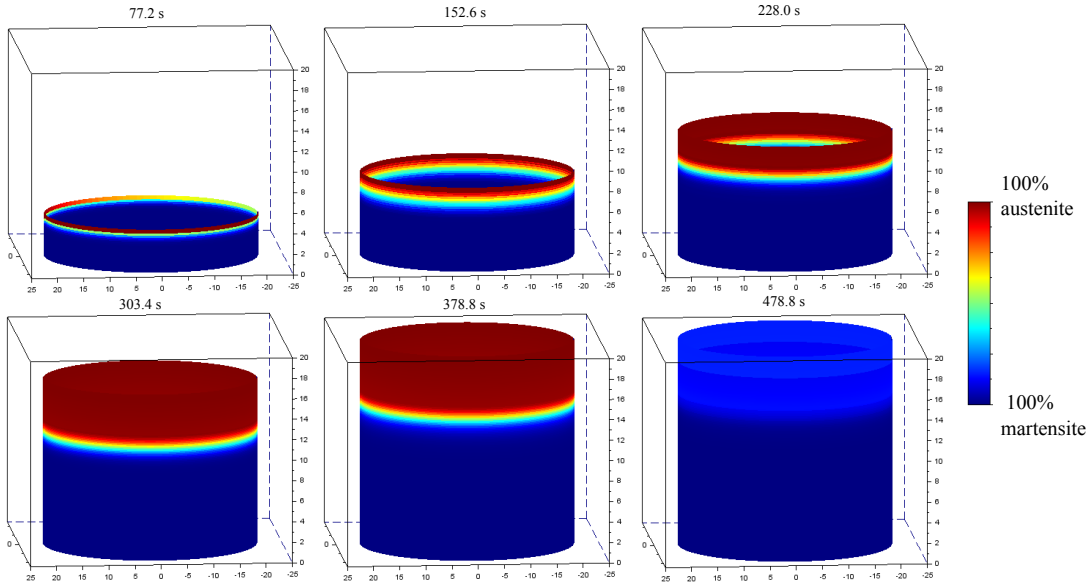


Figure 26: Phase proportion field

## 8. More complex geometry

In this section, the model is applied to a more complex geometry to demonstrate the model capability. A cell of an auxetic is modeled with a continuous path and no dwell time. The cell

geometry is composed of four branches of a Gaussian function as presented in figure 27. This geometry is interesting to test the proposed model as the radius of curvature evolves smoothly on a large interval (see figure 28) and there are four corners (i.e., sharp angles) where the tangent at the path is discontinuous. This discontinuity implies local variation of the laser speed. Indeed, even though the laser speed was set to a fixed value, the machine would need to slow down near the sharp angles in order to follow the imposed trajectory. The laser speed as a function of the curvilinear coordinate (denoted by $l$) is presented in figure 29. (This function has not been measured on a real machine but simply assumed as a possible example). Although the laser speed is not constant along the curvilinear coordinate, the time between two successive metal depositions is constant and reads:

$$t_{n+1} - t_n = \int_0^{l_a} \frac{\mathrm{d}l}{V_{\text{beam}}(l)} \simeq 10 \text{ s} \tag{23}$$

Where $l_a$ is the total length of the auxetic cell. Thus, the effect of the laser speed in the corners is not due to a shorter time between successive metal depositions (as in section 6.3), but to the power brought by the laser and the heat loss due to the gas flow. Indeed, the total energy brought by the laser (or extracted by the gas flow) at a specific computation point increases as the laser speed decreases. Thus, the temperature in the corners is expected to remain higher than the rest of the structure for the layers affected by the laser and cooler than the rest of the structure for the layers affected by the gas flow. This can be verified in figure 30. The specific pattern near the corners has to be validated by in-situ experiments. Infrared pyrometer measurements are likely to be insufficient in the corners, but an infrared camera would enable to test model predictions for relatively complex geometries such as proposed in this section.

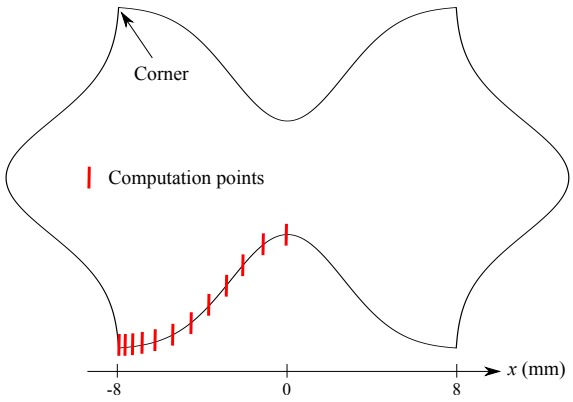


Figure 27: One cell of an auxetic structure

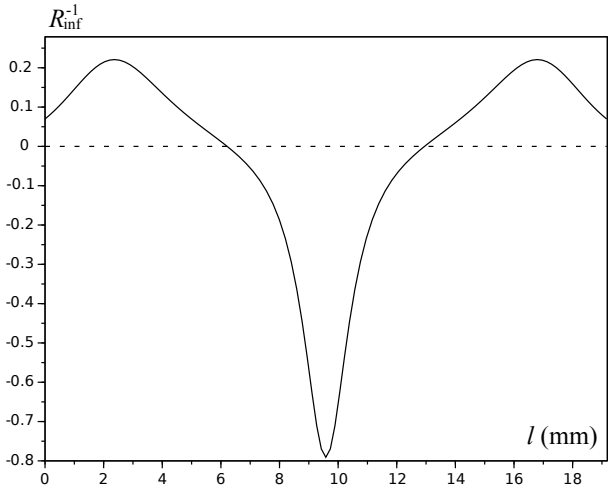


Figure 28: Curvature of one branch of the auxetic geometry

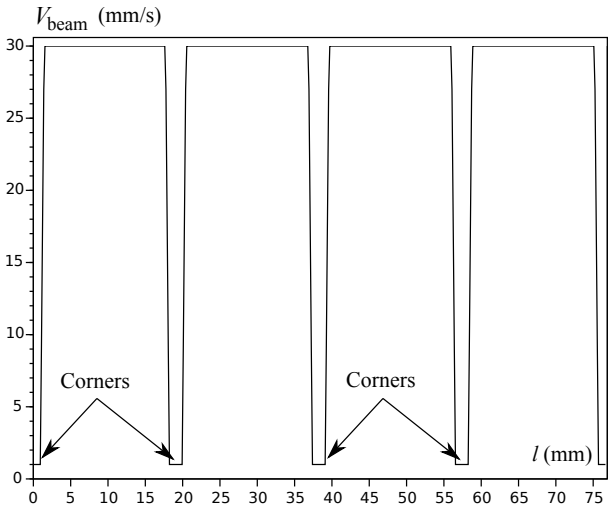


Figure 29: Laser speed as a function of the curvilinear coordinate

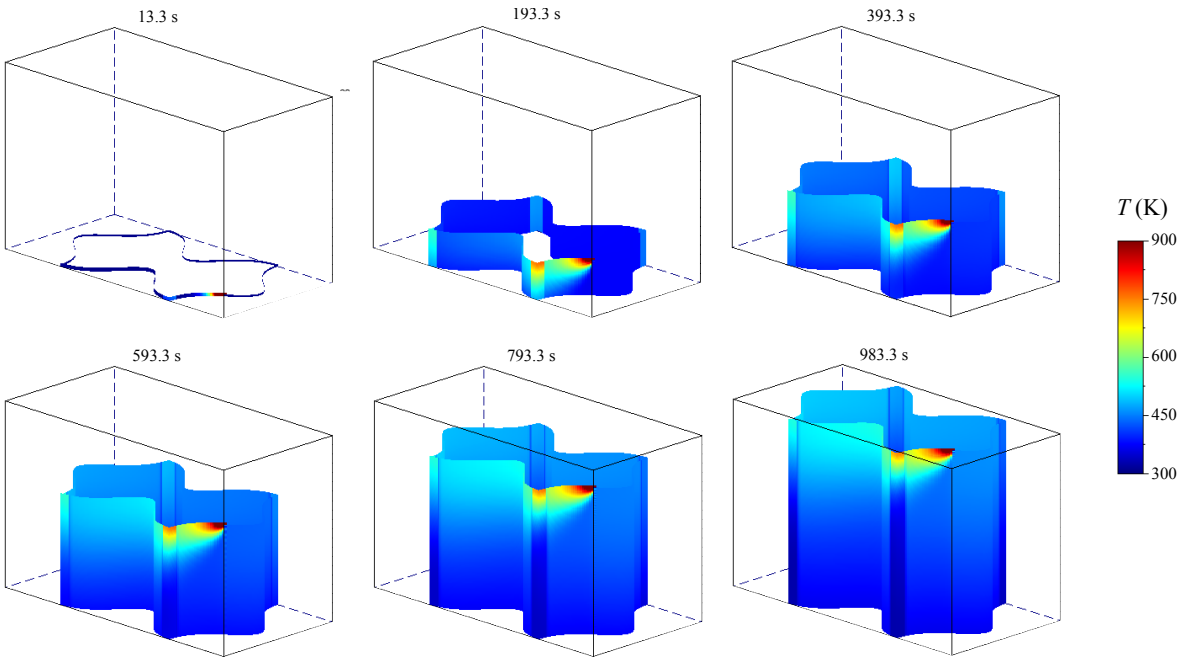


Figure 30: Temperature field for the auxetic geometry

## 9. Conclusion

This paper presents a semi-analytical tool to simulate temperature evolution and phase transitions during directed energy deposition. Phase transitions and latent heat have been considered as well as the power extracted by the gas flow used for carrying the powder. Unlike most of the analytical approaches developed within the framework of additive manufacturing, the proposed model does not rely on classic analytical solutions for moving heat sources in semi-infinite domain. Instead, several 2D multi-layer composites are considered with proper boundary conditions, and combined in order to construct a pseudo-3D temperature field. The modeling strategy is based on the assumption that heat fluxes along the tangent direction to the laser path can be neglected. This assumption is of course questionable in the vicinity of the melt pool, but enables us to obtain reasonable results within short computation time. Indeed, the model has been compared with in-situ pyrometer measurements and good agreement has been observed with 2.6% error in average. Several process parameters have been tested to better control the temperature history and phase changes. This work opens interesting perspectives to predict and control the formation of residual stresses due to thermal expansion and phase transitions. In addition, as the model partially relies on analytic solutions of the nonlinear heat equation, computation time is reduced in comparison to classic finite element techniques. Thus, the proposed model enables us to simulate large structures and perform parametric studies, develop optimization loops and design temperature control devices in order to reach targeted microstructures.

## Acknowledgment

The author acknowledges that Sylvain Durbecq (engineer at Solid Mechanics Laboratory (LMS), École Polytechnique) carried out the in-situ experiment detailed in the paper and would like to thank him for his expertise and fruitful discussion.

## Appendix A. Solution derivation

On each time interval, the material parameters do not depend on temperature. Moreover, for each iteration of the alternating algorithm, the right side term is known. Therefore, the heat conduction equation (6) is linear, and the temperature can be split into three terms:

$$T^{(i)}(r,z,t) = T^{\dagger}(r,z) + T_h^{(i)}(r,z,t) + T_*^{(i)}(r,z,t) \tag{A.1}$$

The steady-state solution is denoted by $T^{\dagger}$ and verifies:

$$\frac{\partial^2 T^{\dagger}}{\partial r^2} + \frac{1}{r}\frac{\partial T^{\dagger}}{\partial r} + \frac{\partial^2 T^{\dagger}}{\partial z^2} = 0 \tag{A.2}$$

With the following boundary conditions:

$$\begin{aligned}
(a): &\begin{cases} \widehat{\lambda}\dfrac{\partial T^{\dagger}}{\partial r} = H\,(T^{\dagger} - T_{\text{ext}}) & r = R_{\text{inf}} \\ \widehat{\lambda}\dfrac{\partial T^{\dagger}}{\partial r} = -H\,(T^{\dagger} - T_{\text{ext}}) & r = R_{\text{sup}} \end{cases} \\
(b): &\begin{cases} \lambda^{(1)}\dfrac{\partial T^{\dagger}}{\partial z} = H_{\text{pla}}\,(T^{\dagger} - T_{\text{pla}}) & z = Z^{(0)} \\ \lambda^{(n)}\dfrac{\partial T^{\dagger}}{\partial z} = -H\,(T^{\dagger} - T_{\text{ext}}) & z = Z^{(n)} \end{cases}
\end{aligned} \tag{A.3}$$

For the sake of simplicity, the condition $(a)$ is verified in a weak sense. Indeed, the thermal conductivities $\lambda^{(i)}$ $(1 \le i \le n)$ have been replaced by their average denoted by $\widehat{\lambda}$. The transient homogenous solution is denoted by $T_h^{(i)}(r,z,t)$ and verifies:

$$\frac{\partial^2 T_h^{(i)}}{\partial r^2} + \frac{1}{r}\frac{\partial T_h^{(i)}}{\partial r} + \frac{\partial^2 T_h^{(i)}}{\partial z^2} - \frac{1}{D^{(i)}}\frac{\partial T_h^{(i)}}{\partial t} = 0 \tag{A.4}$$

With the following boundary conditions:

$$\begin{aligned}
(a): &\begin{cases} \widehat{\lambda}\dfrac{\partial T_h^{(i)}}{\partial r} = H\,T_h^{(i)} & r = R_{\text{inf}} \quad (1 \le i \le n) \\ \widehat{\lambda}\dfrac{\partial T_h^{(i)}}{\partial r} = -H\,T_h^{(i)} & r = R_{\text{sup}} \quad (1 \le i \le n) \end{cases} \\
(b): &\begin{cases} \lambda^{(1)}\dfrac{\partial T_h^{(1)}}{\partial z} = H_{\text{pla}}\,T_h^{(1)} & z = Z^{(0)} \\ \lambda^{(n)}\dfrac{\partial T_h^{(n)}}{\partial z} = -H\,T_h^{(n)} & z = Z^{(n)} \end{cases} \\
(c): &\begin{cases} T_h^{(i)} = T_h^{(i+1)} & z = Z^{(i)} \quad (1 \le i \le n-1) \\ \lambda^{(i)}\dfrac{\partial T_h^{(i)}}{\partial z} = \lambda^{(i+1)}\dfrac{\partial T_h^{(i+1)}}{\partial z} & z = Z^{(i)} \quad (1 \le i \le n-1) \end{cases}
\end{aligned} \tag{A.5}$$

And the particular solution is denoted by $T_*^{(i)}(r,z,t)$ and verifies:

$$\frac{\partial^2 T_*^{(i)}}{\partial r^2} + \frac{1}{r}\frac{\partial T_*^{(i)}}{\partial r} + \frac{\partial^2 T_*^{(i)}}{\partial z^2} - \frac{1}{D^{(i)}}\frac{\partial T_*^{(i)}}{\partial t} = \frac{Q^{(i)}(t)}{\lambda^{(i)}} \tag{A.6}$$

With boundary conditions identical to (A.5) by replacing $T_h^{(i)}$ by $T_*^{(i)}$.

*Appendix A.1. Steady state solution*

A general solution of (A.2) is obtained by separation of variables:

$$T^{\dagger}(r,z) = T_{\text{ext}} + \sum_{j=1}^{N_j} \left(a_j^{\dagger} I_0\left(\alpha_j^{\dagger} r\right) + \widetilde{a}_j^{\dagger} K_0\left(\alpha_j^{\dagger} r\right)\right)\left(b_j^{\dagger}\cos(\alpha_j^{\dagger} z) + \widetilde{b}_j^{\dagger}\sin(\alpha_j^{\dagger} z)\right) \tag{A.7}$$

Where $I_0$, $K_0$ are the zero order modified Bessel functions of the first and second kind respectively. A classic issue of such a solution is that $I_0$ and $K_0$ are extremely similar for sufficiently large values of $r$. This issue leads to a very ill-conditioned matrix. Thus, a simpler solution is preferred, consisting in neglecting the condition $(a)$ in (A.3). This assumption has almost no influence on results mostly because $H_{\text{pla}} \gg H$. Therefore, the solution reduces to:

$$T^{\dagger}(z) = a^{\dagger} z + b^{\dagger} \tag{A.8}$$

Where:

$$\begin{cases} a^{\dagger} = \dfrac{H\, H_{\text{pla}}(T_{\text{ext}} - T_{\text{pla}})}{H(\widehat{\lambda} - H_{\text{pla}}\, Z^{(0)}) + H_{\text{pla}}(\widehat{\lambda} + H\, Z^{(n)})} \\ b^{\dagger} = \dfrac{H(\widehat{\lambda} - H_{\text{pla}}\, Z^{(0)})T_{\text{ext}} + H_{\text{pla}}(\widehat{\lambda} + H\, Z^{(n)})T_{\text{pla}}}{H(\widehat{\lambda} - H_{\text{pla}}\, Z^{(0)}) + H_{\text{pla}}(\widehat{\lambda} + H\, Z^{(n)})} \end{cases} \tag{A.9}$$

*Appendix A.2. Homogeneous solution*

A general solution of (A.5) is obtained by separation of variables:

$$\begin{aligned} T_h^{(i)}(r,z,t) = \; & \sum_{j=1}^{N_j}\sum_{k=1}^{N_k} \Theta_{j,k}\left(a_j J_0\left(\alpha_j r\right) + \widetilde{a}_j Y_0\left(\alpha_j r\right)\right)\left(b_{j,k}^{(i)}\cos(\beta_{j,k}^{(i)} z) + \widetilde{b}_{j,k}^{(i)}\sin(\beta_{j,k}^{(i)} z)\right) \\ & \times \exp\left(-D^{(i)}\left(\alpha_j^2 + \left(\beta_{j,k}^{(i)}\right)^2\right)(t - t_n)\right) \end{aligned} \tag{A.10}$$

Where $J_0$ and $Y_0$ denote the zero order Bessel functions of the first and second kind respectively. Boundary conditions enable to determine the coefficients $a_j, \widetilde{a}_j, b_{j,k}^{(i)}, \widetilde{b}_{j,k}^{(i)}$ and the eigenvalues $\alpha_j, \beta_{j,k}^{(i)}$. The initial condition enables to determine the coefficients $\Theta_{j,k}$ in Appendix A.4. The condition $(a)$ in (A.5) reads:

$$\begin{cases} a_j M_{1,1} + \widetilde{a}_j M_{1,2} = 0 \\ a_j M_{2,1} + \widetilde{a}_j M_{2,2} = 0 \end{cases} \Rightarrow \underbrace{\begin{pmatrix} M_{1,1} & M_{1,2} \\ M_{2,1} & M_{2,2} \end{pmatrix}}_{\boldsymbol{M}(\alpha_j)} \cdot \begin{pmatrix} a_j \\ \widetilde{a}_j \end{pmatrix} = \begin{pmatrix} 0 \\ 0 \end{pmatrix} \tag{A.11}$$

Where:

$$\begin{cases} M_{1,1} = \widehat{\lambda}\alpha_j J_0'\left(\alpha_j R_{\text{inf}}\right) - H J_0\left(\alpha_j R_{\text{inf}}\right) \\ M_{1,2} = \widehat{\lambda}\alpha_j Y_0'\left(\alpha_j R_{\text{inf}}\right) - H Y_0\left(\alpha_j R_{\text{inf}}\right) \\ M_{2,1} = \widehat{\lambda}\alpha_j J_0'\left(\alpha_j R_{\text{sup}}\right) + H J_0\left(\alpha_j R_{\text{sup}}\right) \\ M_{2,2} = \widehat{\lambda}\alpha_j Y_0'\left(\alpha_j R_{\text{sup}}\right) + H Y_0\left(\alpha_j R_{\text{sup}}\right) \end{cases} \tag{A.12}$$

Hence, the eigenvalues $\alpha_j$ are defined as the positive successive roots of the following function:

$$\alpha \mapsto \det\left[\boldsymbol{M}(\alpha)\right] \tag{A.13}$$

Coefficients $a_j$ reads:

$$\begin{cases} a_j = 1 \\ \widetilde{a}_j = -\dfrac{\widehat{\lambda}\alpha_j J_0'\left(\alpha_j R_{\text{inf}}\right) - H J_0\left(\alpha_j R_{\text{inf}}\right)}{\widehat{\lambda}\alpha_j Y_0'\left(\alpha_j R_{\text{inf}}\right) - H Y_0\left(\alpha_j R_{\text{inf}}\right)} \end{cases} \tag{A.14}$$

The continuity of both temperature and heat flux at the interfaces ($\forall\, t \in [t_n, t_{n+1}]$) implies that the time dependance in (A.10) is the same for all layers, thus:

$$D^{(i)}\left(\alpha_j^2 + (\beta_{j,k}^{(i)})^2\right) = D\left(\alpha_j^2 + \beta_{j,k}^2\right) \tag{A.15}$$

Where:

$$D = D^{(i_0)} = \max_{1\leq i\leq n} D^{(i)} \quad \text{and} \quad \beta_{j,k} = \beta_{j,k}^{(i_0)} \tag{A.16}$$

Hence, for $1 \leq i \leq n$:

$$\beta_{j,k}^{(i)} = \sqrt{\frac{D}{D^{(i)}}(\alpha_j^2 + \beta_{j,k}^2) - \alpha_j^2} \tag{A.17}$$

The maximum of the diffusivity has been chosen as a parameter in (A.16) so that the eigenvalues $\beta_{j,k}^{(i)}$ defined in (A.17) are positive. Furthermore, the condition ($b$) in (A.5) reduces to:

$$\begin{cases} b_{j,k}^{(1)} K_{1,1} + \widetilde{b}_{j,k}^{(1)} K_{1,2} = 0 \\ b_{j,k}^{(n)} K_{2n,2n-1} + \widetilde{b}_{j,k}^{(n)} K_{2n,2n} = 0 \end{cases} \tag{A.18}$$

Where:

$$\begin{cases} K_{1,1} = -\lambda^{(1)}\beta_{j,k}^{(1)} \sin(\beta_{j,k}^{(1)} Z^{(0)}) - H_{\text{pla}} \cos(\beta_{j,k}^{(1)} Z^{(0)}) \\ K_{1,2} = \lambda^{(1)}\beta_{j,k}^{(1)} \cos(\beta_{j,k}^{(1)} Z^{(0)}) - H_{\text{pla}} \sin(\beta_{j,k}^{(1)} Z^{(0)}) \\ K_{2n,2n-1} = -\lambda^{(n)}\beta_{j,k}^{(n)} \sin(\beta_{j,k}^{(n)} Z^{(n)}) + H \cos(\beta_{j,k}^{(n)} Z^{(n)}) \\ K_{2n,2n} = \lambda^{(n)}\beta_{j,k}^{(n)} \cos(\beta_{j,k}^{(n)} Z^{(n)}) + H \sin(\beta_{j,k}^{(n)} Z^{(n)}) \end{cases} \tag{A.19}$$

The condition ($c$) in (A.5) reads for $1 \leq i \leq n-1$:

$$\begin{cases} b_{j,k}^{(i)} K_{2i,2i-1} + \widetilde{b}_{j,k}^{(i)} K_{2i,2i} + b_{j,k}^{(i+1)} K_{2i,2i+1} + \widetilde{b}_{j,k}^{(i+1)} K_{2i,2i+2} = 0 \\ b_{j,k}^{(i)} K_{2i+1,2i-1} + \widetilde{b}_{j,k}^{(i)} K_{2i+1,2i} + b_{j,k}^{(i+1)} K_{2i+1,2i+1} + \widetilde{b}_{j,k}^{(i+1)} K_{2i+1,2i+2} = 0 \end{cases} \tag{A.20}$$

Where:

$$\begin{cases} K_{2i,2i-1} = \lambda^{(i)}\beta_{j,k}^{(i)}\cos(\beta_{j,k}^{(i)}Z^{(i)}) \\ K_{2i,2i} = \lambda^{(i)}\beta_{j,k}^{(i)}\sin(\beta_{j,k}^{(i)}Z^{(i)}) \\ K_{2i,2i+1} = -\lambda^{(i)}\beta_{j,k}^{(i)}\cos(\beta_{k}^{(i+1)}Z^{(i)}) \\ K_{2i,2i+2} = -\lambda^{(i)}\beta_{j,k}^{(i)}\sin(\beta_{k}^{(i+1)}Z^{(i)}) \\ K_{2i+1,2i-1} = -\lambda^{(i)}\beta_{j,k}^{(i)}\sin(\beta_{j,k}^{(i)}Z^{(i)}) \\ K_{2i+1,2i} = \lambda^{(i)}\beta_{j,k}^{(i)}\cos(\beta_{j,k}^{(i)}Z^{(i)}) \\ K_{2i+1,2i+1} = \lambda^{(i+1)}\beta_{k}^{(i+1)}\sin(\beta_{k}^{(i+1)}Z^{(i)}) \\ K_{2i+1,2i+2} = -\lambda^{(i+1)}\beta_{k}^{(i+1)}\cos(\beta_{k}^{(i+1)}Z^{(i)}) \end{cases} \tag{A.21}$$

Thus, conditions (A.18) and (A.20) reduce to:

$$\underbrace{\begin{pmatrix} K_{1,1} & K_{1,2} & 0 & 0 & 0 & 0 & \cdots & 0 & 0 & 0 & 0 \\ K_{2,1} & K_{2,2} & K_{2,3} & K_{2,4} & 0 & 0 & \cdots & 0 & 0 & 0 & 0 \\ K_{3,1} & K_{3,2} & K_{3,3} & K_{3,4} & 0 & 0 & \cdots & 0 & 0 & 0 & 0 \\ 0 & 0 & K_{4,3} & K_{4,4} & K_{4,5} & K_{4,6} & \cdots & 0 & 0 & 0 & 0 \\ 0 & 0 & K_{5,3} & K_{5,4} & K_{5,5} & K_{5,6} & \cdots & 0 & 0 & 0 & 0 \\ & & & & & & \vdots & & & & \\ 0 & 0 & 0 & 0 & 0 & 0 & \cdots & K_{2n-2,2n-3} & K_{2n-2,2n-2} & K_{2n-2,2n-1} & K_{2n-2,2n} \\ 0 & 0 & 0 & 0 & 0 & 0 & \cdots & K_{2n-1,2n-3} & K_{2n-1,2n-2} & K_{2n-1,2n-1} & K_{2n-1,2n} \\ 0 & 0 & 0 & 0 & 0 & 0 & \cdots & 0 & 0 & K_{2n,2n-1} & K_{2n,2n} \end{pmatrix}}_{\boldsymbol{K}(\beta_{j,k})} \cdot \begin{pmatrix} b_{j,k}^{(1)} \\ \widetilde{b}_{j,k}^{(1)} \\ \vdots \\ \vdots \\ \vdots \\ \vdots \\ b_{j,k}^{(n)} \\ \widetilde{b}_{j,k}^{(n)} \end{pmatrix} = \begin{pmatrix} 0 \\ \vdots \\ \vdots \\ \vdots \\ \vdots \\ \vdots \\ 0 \end{pmatrix} \tag{A.22}$$

Thus, the eigenvalues $\beta_{j,k}$ are defined as the positive successive roots of the following function:

$$\beta \mapsto \det\left[\boldsymbol{K}(\beta)\right] \tag{A.23}$$

The coefficients $b_{j,k}^{(i)}$ are determined as follows:

$$\begin{cases} b_{j,k}^{(1)} = 1 \\ \widetilde{b}_{j,k}^{(1)} = -\frac{K_{1,1}}{K_{1,2}} b_{j,k}^{(1)} \end{cases} \tag{A.24}$$

The following recursive formula holds for $1 \leq m \leq n-1$:

$$\begin{pmatrix} b_{j,k}^{(i+1)} \\ \widetilde{b}_{j,k}^{(i+1)} \end{pmatrix} = -\begin{pmatrix} K_{2i,2i+1} & K_{2i,2i+2} \\ K_{2i+1,2i+1} & K_{2i+1,2i+2} \end{pmatrix}^{-1} \cdot \begin{pmatrix} K_{2i,2i-1} & K_{2i,2i} \\ K_{2i+1,2i-1} & K_{2i+1,2i} \end{pmatrix} \cdot \begin{pmatrix} b_{j,k}^{(i)} \\ \widetilde{b}_{j,k}^{(i)} \end{pmatrix} \tag{A.25}$$

*Appendix A.3. Particular solution*

For the sake of simplicity, the imposed volumetric heat $Q^{(i)}$ is assumed to be homogenous in each layer (i.e., the volume average of $Q^{(i)}$ is considered in each layer). This assumption is acceptable as each layer is very small. Thus, the imposed volumetric heat $Q^{(i)}$ is approximated as follows:

$$Q^{(i)}(t) \approx \sum_{m=0}^{N_m} \lambda^{(i)}\chi_m^{(i)} \exp\left(-\frac{t-t_n}{\tau_m}\right) \tag{A.26}$$

Where the relaxation times $\tau_m$ are imposed and the coefficients $\chi_m^{(i)}$ are obtained by optimization.

A particular solution of (A.6) verifying the boundary conditions (A.5) may be written in a similar form as (A.10). However, to avoid unnecessary technical developments, weak boundary conditions are considered instead. Indeed, the temperature is replaced by the average temperature on the surface of each layer. More precisely, the weak boundary conditions read:

$$
\begin{aligned}
(a): & \begin{cases} \widehat{\lambda}\dfrac{\partial T_*^{(i)}}{\partial r} = \dfrac{H}{Z^{(i)}-Z^{(i-1)}}\displaystyle\int_{Z^{(i-1)}}^{Z^{(i)}} T_*^{(i)}\mathrm{d}z & r = R_{\mathrm{inf}} \quad (1\le i\le n) \\ \widehat{\lambda}\dfrac{\partial T_*^{(i)}}{\partial r} = -\dfrac{H}{Z^{(i)}-Z^{(i-1)}}\displaystyle\int_{Z^{(i-1)}}^{Z^{(i)}} T_*^{(i)}\mathrm{d}z & r = R_{\mathrm{sup}} \quad (1\le i\le n) \end{cases} \\
(b): & \begin{cases} \lambda^{(1)}\dfrac{\partial T_*^{(1)}}{\partial z} = \dfrac{2H_{\mathrm{pla}}}{R_{\mathrm{sup}}^2-R_{\mathrm{inf}}^2}\displaystyle\int_{R_{\mathrm{inf}}}^{R_{\mathrm{sup}}} rT_*^{(1)}\mathrm{d}r & z = Z^{(0)} \\ \lambda^{(n)}\dfrac{\partial T_*^{(n)}}{\partial z} = -\dfrac{2H}{R_{\mathrm{sup}}^2-R_{\mathrm{inf}}^2}\displaystyle\int_{R_{\mathrm{inf}}}^{R_{\mathrm{sup}}} rT_*^{(n)}\mathrm{d}r & z = Z^{(n)} \end{cases} \\
(c): & \begin{cases} \displaystyle\int_{R_{\mathrm{inf}}}^{R_{\mathrm{sup}}} rT_*^{(i)}\mathrm{d}r = \int_{R_{\mathrm{inf}}}^{R_{\mathrm{sup}}} rT_*^{(i+1)}\mathrm{d}r & z = Z^{(i)} \quad (1\le i\le n-1) \\ \lambda^{(i)}\dfrac{\partial T_*^{(i)}}{\partial z} = \lambda^{(i+1)}\dfrac{\partial T_*^{(i+1)}}{\partial z} & z = Z^{(i)} \quad (1\le i\le n-1) \end{cases}
\end{aligned}
\tag{A.27}
$$

These weak boundary conditions are consistent with the fact that $Q^{(i)}$ has been assumed to be homogenous in each layer. Thus, the particular solution reads:

$$
T_*^{(i)}(r,z,t) = \sum_{m=0}^{N_m}\left[A_m^{(i)}J_0\left(\gamma_m^{(i)}r\right) + \widetilde{A}_m^{(i)}Y_0\left(\gamma_m^{(i)}r\right) + B_m^{(i)}\cos\left(\gamma_m^{(i)}z\right) + \widetilde{B}_m^{(i)}\sin\left(\gamma_m^{(i)}z\right) + U_m^{(i)}\right]\exp\left(-\frac{t-t_n}{\tau_m}\right)
\tag{A.28}
$$

Where $A_m^{(i)}, \widetilde{A}_m^{(i)}, B_m^{(i)}, \widetilde{B}_m^{(i)}$ are coefficients to determine, and:

$$
U_m^{(i)} = \chi_m^{(i)}D^{(i)}\tau_m
\tag{A.29}
$$

And:

$$
\gamma_m^{(i)} = \sqrt{\frac{1}{D^{(i)}\tau_m}}
\tag{A.30}
$$

The condition $(a)$ in (A.27) reads for $1 \le i \le n$:

$$
\begin{cases} A_m^{(i)}K_{2i,4i-3}^* + \widetilde{A}_m^{(i)}K_{2i,4i-2}^* + B_m^{(i)}K_{2i,4i-1}^* + \widetilde{B}_m^{(i)}K_{2i,4i}^* = F_{2i}^* \\ A_m^{(i)}K_{2i+1,4i-3}^* + \widetilde{A}_m^{(i)}K_{2i+1,4i-2}^* + B_m^{(i)}K_{2i+1,4i-1}^* + \widetilde{B}_m^{(i)}K_{2i+1,4i}^* = F_{2i+1}^* \end{cases}
\tag{A.31}
$$

Where:

$$\begin{cases} K^*_{2i,4i-3} = \widehat{\lambda}\gamma_m^{(i)} J_0'\left(\gamma_m^{(i)} R_{\text{inf}}\right) - H J_0\left(\gamma_m^{(i)} R_{\text{inf}}\right) \\ K^*_{2i,4i-2} = \widehat{\lambda}\gamma_m^{(i)} Y_0'\left(\gamma_m^{(i)} R_{\text{inf}}\right) - H Y_0\left(\gamma_m^{(i)} R_{\text{inf}}\right) \\ K^*_{2i,4i-1} = -H C_m^{(i)} \\ K^*_{2i,4i} = -H S_m^{(i)} \\ K^*_{2i+1,4i-3} = \widehat{\lambda}\gamma_m^{(i)} J_0'\left(\gamma_m^{(i)} R_{\text{sup}}\right) + H J_0\left(\gamma_m^{(i)} R_{\text{sup}}\right) \\ K^*_{2i+1,4i-2} = \widehat{\lambda}\gamma_m^{(i)} Y_0'\left(\gamma_m^{(i)} R_{\text{sup}}\right) + H Y_0\left(\gamma_m^{(i)} R_{\text{sup}}\right) \\ K^*_{2i+1,4i-1} = H C_m^{(i)} \\ K^*_{2i+1,4i} = H S_m^{(i)} \end{cases} \tag{A.32}$$

And:

$$\begin{cases} F^*_{2i} = H U_m^{(i)} \\ F^*_{2i+1} = -H U_m^{(i)} \end{cases} \tag{A.33}$$

The condition $(b)$ in (A.27) reads:

$$\begin{cases} A_m^{(1)} K^*_{1,1} + \widetilde{A}_m^{(1)} K^*_{1,2} + B_m^{(1)} K^*_{1,3} + \widetilde{B}_m^{(1)} K^*_{1,4} = F^*_1 \\ A_m^{(n)} K^*_{4n,4n-3} + \widetilde{A}_m^{(n)} K^*_{4n,4n-2} + B_m^{(n)} K^*_{4n,4n-1} + \widetilde{B}_m^{(n)} K^*_{4n,4n} = F^*_{4n} \end{cases} \tag{A.34}$$

Where:

$$\begin{cases} K^*_{1,1} = -H_{\text{pla}} J_m^{(1)} \\ K^*_{1,2} = -H_{\text{pla}} Y_m^{(1)} \\ K^*_{1,3} = -\lambda^{(1)}\gamma_m^{(1)} \sin\left(\gamma_m^{(1)} Z^{(0)}\right) - H_{\text{pla}} \cos\left(\gamma_m^{(1)} Z^{(0)}\right) \\ K^*_{1,4} = \lambda^{(1)}\gamma_m^{(1)} \cos\left(\gamma_m^{(1)} Z^{(0)}\right) - H_{\text{pla}} \sin\left(\gamma_m^{(1)} Z^{(0)}\right) \\ K^*_{4n,4n-3} = H J_m^{(n)} \\ K^*_{4n,4n-2} = H Y_m^{(n)} \\ K^*_{4n,4n-1} = -\lambda^{(n)}\gamma_m^{(n)} \sin\left(\gamma_m^{(n)} Z^{(n)}\right) + H \cos\left(\gamma_m^{(n)} Z^{(n)}\right) \\ K^*_{4n,4n} = \lambda^{(n)}\gamma_m^{(n)} \cos\left(\gamma_m^{(n)} Z^{(n)}\right) + H \sin\left(\gamma_m^{(n)} Z^{(n)}\right) \end{cases} \tag{A.35}$$

And:

$$\begin{cases} F^*_1 = H_{\text{pla}} U_m^{(1)} \\ F^*_{4n} = -H U_m^{(n)} \end{cases} \tag{A.36}$$

The condition $(c)$ in (A.27) reads for $1 \leq i \leq n-1$:

$$\begin{cases} A_m^{(i)} K^*_{2n+2i,4i-3} + \widetilde{A}_m^{(i)} K^*_{2n+2i,4i-2} + B_m^{(i)} K^*_{2n+2i,4i-1} + \widetilde{B}_m^{(i)} K^*_{2n+2i,4i} \\ + A_m^{(i+1)} K^*_{2n+2i,4i+1} + \widetilde{A}_m^{(i+1)} K^*_{2n+2i,4i+2} + B_m^{(i+1)} K^*_{2n+2i,4i+3} + \widetilde{B}_m^{(i+1)} K^*_{2n+2i,4i+4} = F^*_{2n+2i} \\ B_m^{(i)} K^*_{2n+2i+1,4i-1} + \widetilde{B}_m^{(i)} K^*_{2n+2i+1,4i} + B_m^{(i+1)} K^*_{2n+2i+1,4i+3} + \widetilde{B}_m^{(i+1)} K^*_{2n+2i+1,4i+4} = F^*_{2n+2i+1} \end{cases} \tag{A.37}$$

Where:

$$\begin{cases} K^*_{2n+2i,4i-3} = \lambda^{(i)}\gamma_m^{(i)} J_m^{(i)} \\ K^*_{2n+2i,4i-2} = \lambda^{(i)}\gamma_m^{(i)} Y_m^{(i)} \\ K^*_{2n+2i,4i-1} = \lambda^{(i)}\gamma_m^{(i)} \cos\left(\gamma_m^{(i)} Z^{(i)}\right) \\ K^*_{2n+2i,4i} = \lambda^{(i)}\gamma_m^{(i)} \sin\left(\gamma_m^{(i)} Z^{(i)}\right) \\ K^*_{2n+2i,4i+1} = -\lambda^{(i)}\gamma_m^{(i)} J_m^{(i+1)} \\ K^*_{2n+2i,4i+2} = -\lambda^{(i)}\gamma_m^{(i)} Y_m^{(i+1)} \\ K^*_{2n+2i,4i+3} = -\lambda^{(i)}\gamma_m^{(i)} \cos\left(\gamma_m^{(i+1)} Z^{(i)}\right) \\ K^*_{2n+2i,4i+4} = -\lambda^{(i)}\gamma_m^{(i)} \sin\left(\gamma_m^{(i+1)} Z^{(i)}\right) \\ K^*_{2n+2i+1,4i-1} = -\lambda^{(i)}\gamma_m^{(i)} \sin\left(\gamma_m^{(i)} Z^{(i)}\right) \\ K^*_{2n+2i+1,4i} = \lambda^{(i)}\gamma_m^{(i)} \cos\left(\gamma_m^{(i)} Z^{(i)}\right) \\ K^*_{2n+2i+1,4i+3} = \lambda^{(i+1)}\gamma_m^{(i+1)} \sin\left(\gamma_m^{(i+1)} Z^{(i)}\right) \\ K^*_{2n+2i+1,4i+4} = -\lambda^{(i+1)}\gamma_m^{(i+1)} \cos\left(\gamma_m^{(i+1)} Z^{(i)}\right) \end{cases} \tag{A.38}$$

And:

$$\begin{cases} F^*_{2n+2i} = \lambda^{(i)}\gamma_m^{(i)} \left(U_m^{(i+1)} - U_m^{(i)}\right) \\ F^*_{2n+2i+1} = 0 \end{cases} \tag{A.39}$$

Where the following quantities have been introduced:

$$\begin{cases} C_m^{(i)} = \dfrac{1}{Z^{(i)} - Z^{(i-1)}} \displaystyle\int_{Z^{(i-1)}}^{Z^{(i)}} \cos\left(\gamma_m^{(i)} z\right) \mathrm{d}z \\ S_m^{(i)} = \dfrac{1}{Z^{(i)} - Z^{(i-1)}} \displaystyle\int_{Z^{(i-1)}}^{Z^{(i)}} \sin\left(\gamma_m^{(i)} z\right) \mathrm{d}z \\ J_m^{(i)} = \dfrac{2}{R_{\mathrm{sup}}^2 - R_{\mathrm{inf}}^2} \displaystyle\int_{R_{\mathrm{inf}}}^{R_{\mathrm{sup}}} r J_0\left(\gamma_m^{(i)} r\right) \mathrm{d}r \\ Y_m^{(i)} = \dfrac{2}{R_{\mathrm{sup}}^2 - R_{\mathrm{inf}}^2} \displaystyle\int_{R_{\mathrm{inf}}}^{R_{\mathrm{sup}}} r Y_0\left(\gamma_m^{(i)} r\right) \mathrm{d}r \end{cases} \tag{A.40}$$

Consider $\boldsymbol{X} = \left(A_m^{(1)}, \widetilde{A}_m^{(1)}, B_m^{(1)}, \widetilde{B}_m^{(1)}, \cdots, A_m^{(n)}, \widetilde{A}_m^{(n)}, B_m^{(n)}, \widetilde{B}_m^{(n)}\right)$, and $\boldsymbol{F}^*$ and $\boldsymbol{K}^*$ the vector and second order tensor, respectively defined by (A.33), (A.36), (A.39) and (A.32), (A.35), (A.38). Coefficients are obtained as follows:

$$\boldsymbol{X} = [\boldsymbol{K}^*]^{-1} . \boldsymbol{F}^* \tag{A.41}$$

*Appendix A.4. Initial condition*

The only remaining unknowns are the coefficients $\Theta_{j,k}$. The initial condition (10) is used to determine these coefficients. The following scalar product is needed:

$$\langle f_1, f_2 \rangle = \sum_{i=1}^{n} \frac{\lambda^{(i)}}{D^{(i)}} \int_{Z^{(i)}}^{Z^{(i+1)}} \int_{R_{\mathrm{inf}}}^{R_{\mathrm{sup}}} r f_1(r,z) f_2(r,z) \mathrm{d}r\mathrm{d}z \tag{A.42}$$

Consider the function basis defined on the entire multilayer structure:

$$f_{j,k} : (r,z) \mapsto \left(a_j J_0\left(\alpha_j\, r\right) + \widetilde{a}_j Y_0\left(\alpha_j\, r\right)\right)\left(b_{j,k}^{(i)} \cos(\beta_{j,k}^{(i)}\, z) + \widetilde{b}_{j,k}^{(i)} \sin(\beta_{j,k}^{(i)}\, z)\right) \tag{A.43}$$

Where the layer $(i)$ is selected accordingly to $z$. The following orthogonality rule holds:

$$\left\langle f_{j,k}, f_{j',k'} \right\rangle = \begin{cases} \left\langle f_{j,k}, f_{j,k} \right\rangle > 0 & \text{if} \quad j = j' \quad \text{and} \quad k = k' \\ 0 & \text{if} \quad j \neq j' \quad \text{or} \quad k \neq k' \end{cases} \tag{A.44}$$

Thus, the initial condition (10) reads:

$$\sum_{j=1}^{N_j} \sum_{k=1}^{N_k} \Theta_{j,k} f_{j,k}(r,z) = T_{\text{ini}}(r,z) - T^{\dagger}(r,z) - T_*(r,z,t_n) = T_0(r,z) \tag{A.45}$$

Where:

$$T_* : (r,z,t) \mapsto \begin{cases} T_*^{(i)}(r,z,t) \\ \text{for } z \in \left[Z^{(i-1)}, Z^{(i)}\right] \end{cases} \tag{A.46}$$

The coefficients $\Theta_{j,k}$ are determined as follows:

$$\Theta_{j,k} = \frac{\left\langle f_{j,k}, T_0 \right\rangle}{\left\langle f_{j,k}, f_{j,k} \right\rangle} \tag{A.47}$$

## References


[1] I. Gibson, D. Rosen, B. Stucker, Directed energy deposition processes, in: Additive Manufacturing Technologies, Springer, 2015, pp. 245–268.

[2] D. Gu, W. Meiners, K. Wissenbach, R. Poprawe, Laser additive manufacturing of metallic components: materials, processes and mechanisms, International materials reviews 57 (2012) 133–164.

[3] M. Somashekara, M. Naveenkumar, A. Kumar, C. Viswanath, S. Simhambhatla, Investigations into effect of weld-deposition pattern on residual stress evolution for metallic additive manufacturing, The International Journal of Advanced Manufacturing Technology 90 (2017) 2009–2025.

[4] J. S. Panchagnula, S. Simhambhatla, Manufacture of complex thin-walled metallic objects using weld-deposition based additive manufacturing, Robotics and Computer-Integrated Manufacturing 49 (2018) 194–203.

[5] W. E. Frazier, Metal additive manufacturing: a review, Journal of Materials Engineering and Performance 23 (2014) 1917–1928.

[6] T. DebRoy, H. Wei, J. Zuback, T. Mukherjee, J. Elmer, J. Milewski, A. M. Beese, A. Wilson-Heid, A. De, W. Zhang, Additive manufacturing of metallic components–process, structure and properties, Progress in Materials Science 92 (2018) 112–224.

[7] X. Zhao, J. Chen, X. Lin, W. Huang, Study on microstructure and mechanical properties of laser rapid forming inconel 718, Materials Science and Engineering: A 478 (2008) 119–124.

[8] V. Manvatkar, A. De, T. DebRoy, Heat transfer and material flow during laser assisted multi-layer additive manufacturing, Journal of Applied Physics 116 (2014) 124905.

[9] W. J. Sames, F. List, S. Pannala, R. R. Dehoff, S. S. Babu, The metallurgy and processing science of metal additive manufacturing, International Materials Reviews 61 (2016) 315–360.

[10] D. Carron, P. Le Masson, R. Fabbro, 2d longitudinal modeling of heat transfer and fluid flow during multilayered direct laser metal deposition process, JOURNAL (OF LASER APPLICATIONS 24 (2012).

[11] A. Yadollahi, N. Shamsaei, S. M. Thompson, D. W. Seely, Effects of process time interval and heat treatment on the mechanical and microstructural properties of direct laser deposited 316l stainless steel, Materials Science and Engineering: A 644 (2015) 171–183.

[12] V. Manvatkar, A. De, T. DebRoy, Spatial variation of melt pool geometry, peak temperature and solidification parameters during laser assisted additive manufacturing process, Materials Science and Technology 31 (2015) 924–930.

[13] M. Megahed, H.-W. Mindt, N. NDri, H. Duan, O. Desmaison, Metal additive-manufacturing process and residual stress modeling, Integrating Materials and Manufacturing Innovation 5 (2016) 61–93.

[14] E. Kundakcioglu, I. Lazoglu, S. Rawal, Transient thermal modeling of laser-based additive manufacturing for 3d freeform structures, The International Journal of Advanced Manufacturing Technology 85 (2016) 493–501.

[15] Y. Lian, S. Lin, W. Yan, W. K. Liu, G. J. Wagner, A parallelized three-dimensional cellular automaton model for grain growth during additive manufacturing, Computational Mechanics 61 (2018) 543–558.

[16] H. Wei, G. Knapp, T. Mukherjee, T. DebRoy, Three-dimensional grain growth during multi-layer printing of a nickel-based alloy inconel 718, Additive Manufacturing 25 (2019) 448–459.

[17] C. Kumara, A. Segerstark, F. Hanning, N. Dixit, S. Joshi, J. Moverare, P. Nylén, Microstructure modelling of laser metal powder directed energy deposition of alloy 718, Additive Manufacturing 25 (2019) 357–364.

[18] W. Yan, S. Lin, O. L. Kafka, Y. Lian, C. Yu, Z. Liu, J. Yan, S. Wolff, H. Wu, E. Ndip-Agbor, et al., Data-driven multi-scale multi-physics models to derive process–structure–property relationships for additive manufacturing, Computational Mechanics 61 (2018) 521–541.

[19] E. R. Denlinger, J. C. Heigel, P. Michaleris, T. Palmer, Effect of inter-layer dwell time on distortion and residual stress in additive manufacturing of titanium and nickel alloys, Journal of Materials Processing Technology 215 (2015) 123–131.

[20] E. R. Denlinger, P. Michaleris, Effect of stress relaxation on distortion in additive manufacturing process modeling, Additive Manufacturing 12 (2016) 51–59.

[21] Z. Wang, T. A. Palmer, A. M. Beese, Effect of processing parameters on microstructure and tensile properties of austenitic stainless steel 304l made by directed energy deposition additive manufacturing, Acta Materialia 110 (2016) 226–235.

[22] B. A. Szost, S. Terzi, F. Martina, D. Boisselier, A. Prytuliak, T. Pirling, M. Hofmann, D. J. Jarvis, A comparative study of additive manufacturing techniques: Residual stress and microstructural analysis of clad and waam printed ti–6al–4v components, Materials & Design 89 (2016) 559–567.

[23] M. Biegler, B. Graf, M. Rethmeier, In-situ distortions in lmd additive manufacturing walls can be measured with digital image correlation and predicted using numerical simulations, Additive Manufacturing 20 (2018) 101–110.

[24] X. Lu, X. Lin, M. Chiumenti, M. Cervera, Y. Hu, X. Ji, L. Ma, H. Yang, W. Huang, Residual stress and distortion of rectangular and s-shaped ti-6al-4v parts by directed energy deposition: modelling and experimental calibration, Additive Manufacturing 26 (2019) 166–179.

[25] L. Wang, S. D. Felicelli, J. E. Craig, Thermal modeling and experimental validation in the lens tm process, in: 18th Solid Freeform Fabrication Symposium. Austin, TX, pp. 100–111.

[26] H. Liu, Numerical analysis of thermal stress and deformation in multi-layer laser metal deposition process, Ph.D. thesis, Missouri University of Science and Technology, 2014.

[27] G. Marion, G. Cailletaud, C. Colin, M. Mazière, A finite element model for the simulation of direct metal deposition, in: International Congress on Applications of Lasers & Electro-Optics, volume 1, LIA, pp. 834–841.

[28] J. Smith, W. Xiong, J. Cao, W. K. Liu, Thermodynamically consistent microstructure prediction of additively manufactured materials, Computational mechanics 57 (2016) 359–370.

[29] T. Keller, G. Lindwall, S. Ghosh, L. Ma, B. M. Lane, F. Zhang, U. R. Kattner, E. A. Lass, J. C. Heigel, Y. Idell, et al., Application of finite element, phase-field, and calphad-based methods to additive manufacturing of ni-based superalloys, Acta materialia 139 (2017) 244–253.

[30] Q. Chen, G. Guillemot, C.-A. Gandin, M. Bellet, Three-dimensional finite element thermomechanical modeling of additive manufacturing by selective laser melting for ceramic materials, Additive Manufacturing 16 (2017) 124–137.

[31] D. Zhang, Z. Feng, C. Wang, Z. Liu, D. Dong, Y. Zhou, R. Wu, Modeling of temperature field evolution during multilayered direct laser metal deposition, Journal of Thermal Spray Technology 26 (2017) 831–845.

[32] C. Baykasoglu, O. Akyildiz, D. Candemir, Q. Yang, A. C. To, Predicting microstructure evolution during directed energy deposition additive manufacturing of ti-6al-4v, Journal of Manufacturing Science and Engineering 140 (2018) 051003.

[33] B. Zheng, Y. Zhou, J. Smugeresky, J. Schoenung, E. Lavernia, Thermal behavior and microstructural evolution during laser deposition with laser-engineered net shaping: Part i. numerical calculations, Metallurgical and materials transactions A 39 (2008) 2228–2236.

[34] T. Moran, P. Li, D. Warner, N. Phan, Utility of superposition-based finite element approach for part-scale thermal simulation in additive manufacturing, Additive Manufacturing 21 (2018) 215–219.

[35] Y. Yang, M. Knol, F. Van Keulen, C. Ayas, A semi-analytical thermal modelling approach for selective laser melting, Additive Manufacturing 21 (2018) 284–297.

[36] J. Ning, D. E. Sievers, H. Garmestani, S. Y. Liang, Analytical modeling of transient temperature in powder feed metal additive manufacturing during heating and cooling stages, Applied Physics A 125 (2019) 496.

[37] J. Ning, E. Mirkoohi, Y. Dong, D. E. Sievers, H. Garmestani, S. Y. Liang, Analytical modeling of 3d temperature distribution in selective laser melting of ti-6al-4v considering part boundary conditions, Journal of Manufacturing Processes 44 (2019) 319–326.

[38] A. J. Wolfer, J. Aires, K. Wheeler, J.-P. Delplanque, A. Rubenchik, A. Anderson, S. Khairallah, Fast solution strategy for transient heat conduction for arbitrary scan paths in additive manufacturing, Additive Manufacturing (2019) 100898.

[39] J. Li, Q. Wang, P. P. Michaleris, An analytical computation of temperature field evolved in directed energy deposition, Journal of Manufacturing Science and Engineering 140 (2018) 101004.

[40] D. Rosenthal, The theory of moving sources of heat and its application of metal treatments, Transactions of ASME 68 (1946) 849–866.

[41] F. De Monte, Unsteady heat conduction in two-dimensional two slab-shaped regions. exact closed-form solution and results, International Journal of Heat and Mass Transfer 46 (2003) 1455–1469.

[42] D. Weisz-Patrault, Coupled heat conduction and multiphase change problem accounting for thermal contact resistance, International Journal of Heat and Mass Transfer 104 (2017) 595–606.

[43] Scilab, Scilab 6.0.0: Free and open source software for numerical computation, Scilab Enterprises, Orsay, France (2019).

[44] W. A. Johnson, R. F. Mehl, Reaction kinetics in processes of nucleation and growth, Trans. Aime 135 (1939) 396–415.

[45] M. Avrami, Kinetics of phase change. i general theory, The Journal of Chemical Physics 7 (1939) 1103–1112.

[46] M. Avrami, Kinetics of phase change. ii transformation-time relations for random distribution of nuclei, The Journal of Chemical Physics 8 (1940) 212–224.

[47] M. Avrami, Kinetics of phase change. iii. granulation, phase change, and microstructure, The Journal of chemical physics 9 (1941) 177–184.

[48] D. Koistinen, R. Marburger, A general equation prescribing the extent of the austenite-martensite transformation in pure iron-carbon alloys and plain carbon steels, acta metallurgica 7 (1959) 59–60.

[49] H. Li, K. Gai, L. He, C. Zhang, H. Cui, M. Li, Non-isothermal phase-transformation kinetics model for evaluating the austenization of 55crmo steel based on johnson–mehl–avrami equation, Materials & Design 92 (2016) 731–741.

[50] X. Luo, L. Han, J. Gu, Study on austenitization kinetics of sa508 gr. 3 steel based on isoconversional method, Metals 6 (2016) 8.

[51] AZoM.com, Azo materials: Stainless steel - grade 316 (uns s31600), https://www.azom.com/article.aspx?ArticleID=2382, 2019. Accessed: 2019-06-7.

[52] S. Kou, Welding metallurgy, New Jersey, USA (2003) 431–446.

[53] H. Wei, J. Mazumder, T. DebRoy, Evolution of solidification texture during additive manufacturing, Scientific reports 5 (2015) 16446.